Naval Research Laboratory

Simulations of Hypersonic Rarefied Gas Flows Using DSMC-MLG

THUONG X. NGUYEN
CHOONG K. OH
ROBERT S. SINKOVITS
ELAINE S. ORAN

Laboratory for Computational Physics and Fluid Dynamics

JOHN D. ANDERSON, JR.

Department of Aerospace Engineering
University of Maryland, College Park

19970527 112

May 16, 1997

REPORT DOCUMENTATION PAGE

1. AGENCY USE ONLY (Leave Blank)	2. REPORT DATE	3. REPORT TYPE AND DATES COVERED
	May 16, 1997	

4. TITLE AND SUBTITLE

Simulations of Hypersonic Rarefied Gas Flows Using DSMC-MLG

5. FUNDING NUMBERS

PE - 62702E

6. AUTHOR(S)

T.X. Nguyen, C.K. Oh, R.S. Sinkovits, J.D. Anderson, Jr.,* and E.S. Oran

7. PERFORMING ORGANIZATION NAME(S) AND ADDRESS(ES)

Naval Research Laboratory
Washington, DC 20375-5320

8. PERFORMING ORGANIZATION REPORT NUMBER

NRL/MR/6404--97-7917

9. SPONSORING/MONITORING AGENCY NAME(S) AND ADDRESS(ES)

ONR, 800 North Quincy St., Arlington, VA 22217-5660
DARPA, 3701 N. Fairfax Dr., Arlington, VA 22203-1714

10. SPONSORING/MONITORING AGENCY REPORT NUMBER

11. SUPPLEMENTARY NOTES

*Department of Aerospace Engineering
University of Maryland, College Park

12a. DISTRIBUTION/AVAILABILITY STATEMENT

Approved for public release; distribution unlimited.

12b. DISTRIBUTION CODE

13. ABSTRACT (Maximum 200 words)

The combined Direct Simulation Monte Carlo (DSMC) and Monotonic Lagrangian Grid (MLG) methodologies are used on the massively parallel Connection Machines CM-5 to solve for the properties of a low-density hypersonic flow through a channel containing a wedge. Numerical issues related to grid generation around the obstacle, the effects of resolution in terms of the simulated to actual particle ratio, and the use of time-averaging to obtain a statistically converged solution are discussed. A method is presented for quantifying the effects of the grid on the solution. The flow field shows many important aerodynamic features, such as shock waves, boundary layers, expansion fan, and their interactions. Since the flow is so rarefied, these structures are diffuse compared to what is expected in a continuum flow. For example, the reattachment shock behind the trailing edge of the wedge degenerates into a diffuse viscous layer. Other low-density effects include the velocity slip, which peaks near the leading edges where the density is low, and temperature jump of the gas adjacent to the solid surfaces, which is highest at the entrance of the channel and decreases further downstream. The calculated skin friction and heat transfer agree well with the Reynolds analogy for boundary-layer flow. The computed pressure distributions along the wall are consistent with hypersonic viscous theory and other DSCMC calculations.

14. SUBJECT TERMS		15. NUMBER OF PAGES
Hypersonic	DSMC-MLG	64
Rarefied gas dynamics		16. PRICE CODE

17. SECURITY CLASSIFICATION OF REPORT	18. SECURITY CLASSIFICATION OF THIS PAGE	19. SECURITY CLASSIFICATION OF ABSTRACT	20. LIMITATION OF ABSTRACT
UNCLASSIFIED	UNCLASSIFIED	UNCLASSIFIED	UL

CONTENTS

SIMULATIONS OF HYPERSONIC RAREFIED GAS FLOWS USING DSMC-MLG

1   INTRODUCTION

Under transitional-flow conditions, the gradients of the macroscopic variables become so steep that their scale length, L, is on the order of the average mean free path, λ. When the Knudsen number, $Kn = \lambda/L$, is large ($Kn > 0.03$), the standard Navier-Stokes (NS) formulation cannot be used because the constitutive relations used in the continuum formulation are not valid. For the cases where $Kn < 0.2$, extensive efforts have been made to modify both the boundary conditions and the constitutive relations for the Navier-Stokes equations (Probstein and Pan, 1963; Oguchi, 1963; Pan and Probstein, 1966; Kogan, 1969; Beskok and Karniadakis, 1994) to extend the range of application of the continuum formulation to the transitional regime. However, the continuum approach, even with the modified input or formulation, can only be used over a very small range $0.03 < Kn < 0.2$. For $Kn > 0.2$, it becomes necessary to use a molecular approach, such as molecular dynamics (Allen and Tildesley, 1990), a Boltzmann equation solution method (Bhatnagar et al., 1954), or a statistical molecular method such as Direct Simulation Monte Carlo (Bird, 1963).

The Direct Simulation Monte Carlo (DSMC) method is an approach that has been used widely and successfully to predict the properties of transitional-regime flows. This is a numerical particle-simulation technique based on kinetic theory. The gas is represented by a large collection of discrete particles, which are subject to intermolecular collisions and molecule-surface interactions. Statistical accuracy is obtained by averaging the results over many independent simulations, which may be simplified to time-averaging for steady flows. DSMC has been applied extensively to describe reentry flows (Moss and Bird, 1984; Moss, 1986; Bird, 1987; Moss et al., 1988; Bird, 1990), shock interaction on vehicles at high altitudes (Carlson and Wilmoth, 1992), and flows over waveriders (Rault, 1992). More recently, DSMC has been extended to microdynamical flows, such as microchannels used in MEMS devices (Oh et al., 1995; Nguyen et al., 1996), and to chemically reacting flows (Dogra et al., 1994). DSMC has been shown to be equivalent to solving the Boltzmann equation for problems involving monatomic gases undergoing binary collisions (Nanbu, 1982).

The DSMC can require very large amounts of computational time and memory to compute the properties of systems with realistic sizes and densities. The computational time required is directly proportional to N, where N is the number of simulated particles. Because the statistical error reduces as $1/\sqrt{N}$, a large number of samples must be collected and averaged to reduce the statistical noise. The value of N also determines the grid resolution. For three-dimensional flows, or flow with gradients that need high local resolution, the use of DSMC becomes extremely limited by available computer resources. Recent attempts to reduce computational time have involved both using massively parallel computers to handle many particles (Furlani and Lordi, 1989; Wilmoth, 1989; Goldstein and Sturtevant, 1989; Dagum, 1991) and applications of new particle tracking methods (Cybyk et al., 1995).

In a conventional DSMC calculation, the computational domain is divided into a grid of spatially fixed cells. However, this approach may result in incorrect prediction of collision rates within sparsely populated cells. In addition, the requirement of small cell sizes in regions of large macroscopic gradients (such as shock structures and boundary layers) may be violated at later sampling times. Both of these problems are resolved by combining the DSMC with the Monotonic Lagrangian Grid (MLG), an algorithm for optimizing particle tracking and sorting (Cybyk, 1994). The MLG (Boris, 1986) is a particle sorting method that ensures that particles that are adjacent in physical space are also adjacent in index space. This means that, given the location of a particle in space (x,y) with array indices (i,j), all of the nearest neighbors of this particle are offset by at most a few indices in any direction. This is achieved by continually changing the location of data in computer memory. The method is easily optimized on most of types of computers, and is extremely efficient on massively parallel computers (Oh et al., 1996b). Combining the DSMC and the MLG eliminates the fixed spatial grid of the conventional DSMC approach, and results in a method that allows automatic grid refinement according to the local number density of the gas, which in turn produces higher accuracy for a given grid size (Cybyk et al., 1995).

In this paper, the combined DSMC-MLG is used on the massively parallel Connection

Machines to examine the hypersonic, transitional-regime flow through a channel with a wedge on the bottom surface. In the past, there have been related studies of hypersonic, high-Kn flows on ramps and cones. For example, there have been DSMC calculations of flows over a two-dimensional ramp that studied the pressure distribution along the ramp surface (Moss et al., 1991), and shock/boundary-layer interactions as a function of ramp angle (Chpoun et al., 1993). A study of flows over sharp cones (Taylor et al., 1989) showed that the wake has minimal effects on the flow properties along the forebody of the cone, suggesting a similar behaviour in the wedge case. These studies address parts of the physics in the problem analyzed below.

Figure 1 is a sketch of the typical flow that would be expected for continuum conditions. Oblique shocks start at the leading edges of the channel and the wedge, interact with each other, and compress the flow above the slanted part of the wedge (the wedge forebody). The trailing edge of the wedge acts as a backward facing step, so that the flow expands past the step to extremely low density. The rarefied gas effects, and the inaccuracies of the NS formulation, may be most significant in this region. Downstream of the wedge, the flow turns parallel to the channel and forms a reattachment shock. The adverse pressure gradient across this shock causes the boundary layer to separate and the flow reverses direction. Thus a recirculating region is created behind the wedge. These flow features, effected by the reflected and refracted shocks, are expected to change for a rarefied flow.

From a fluid dynamic standpoint, the channel-wedge geometry produces a flow field with many important aerodynamic features (such as shock waves, expansion fan, and boundary layers) and their complex interactions, which are not yet well understood for rarefied conditions. This study shows the effects of rarefied conditions on the flow structures by comparing the computational results qualitatively to what would be expected in a continuum flow in Figure 1. Distributions of macroscopic properties in the flow field are examined. The shear stress and thermal loading on the solid surfaces are calculated and their relationship in terms of the Reynolds analogy is shown. The computed results are then compared to

3

existing theoretical and computational data.

From an algorithmic standpoint, the problem studied here expands the application of DSMC-MLG to more complex geometry than the channel flows for which it was previously used. It is thus possible to test and develop aspects of the combined method, and arrive at improved boundary conditions and more specific information or the requirements for convergence and the effects of the quality of the grid on the solution. In particular, we discuss the problems of generating a grid around the wedge and describe a method for selecting the best grid. Then we describe detailed resolution tests in which the grid is successively refined and the solutions are compared. We also evaluate what is required to obtain statistically converged solution when the time-averaging process is used.

2 COMPUTATIONAL METHOD

2.1 Direct Simulation Monte Carlo

The procedures for a conventional DSMC (Bird, 1963) calculation are shown in the flowchart in Figure 2. The computational domain is first divided into spatially fixed cells system. The particles are then randomly distributed in the computational domain. These simulated particles, each representing one or more real gas molecules, are assigned random velocities that are usually based on the equilibrium distribution of an undisturbed gas. To begin the simulation, the representative particles are moved for a convection timestep of magnitude Δt_g. This molecular-motion process is modeled deterministically. During this step, interactions between molecules and the solid boundaries are simulated, and macroscopic properties along the solid surfaces can be calculated.

The next step involves tracking and indexing all particles. New positions of the molecules are sorted. This step, however, is a very time-consuming part of the simulation where particles in physical space must first be indexed in computer memory, and their cell locations must be determined before collision pairs are selected. This step is where the addition of the MLG algorithm provides significant computational benefits.

The molecular-collision process is modeled probabilistically. Only particles within a given grid cell are considered as possible collision partners. Within each cell, a representative set of collisions is simulated, and collision pairs are selected randomly. The post-collision velocities are determined before particles are allowed to move for the next Δt_g. This process of uncoupling molecular motions and intermolecular collisions requires that Δt_g must be smaller than the mean collision time of the unperturbed gas.

There are serveral collision sampling methods that have been used successfully. Of those, the time-counter (TC) technique and the no-time-counter (NTC) technique (Bird, 1976; Bird, 1989) are most commonly used. It has been found that the TC method allows the acceptance of unlikely collision pairs which results in inaccurate collision rates. In this study, we use the NTC technique which corrects this problem.

At selected time intervals Δt_s, the macroscopic properties, such as density, temperature, and pressure may be sampled. The average of these properties are calculated at the geometric centers of the grid cells. When the actual-to-simulated molecule ratio, S_m, is large, there is a high level of statistical scattering in the results, and either ensemble-averaging or time-averaging is needed to reduce the statistical fluctuations.

2.2 Monotonic Lagrangian Grid

The criteria ensuring that particles which are adjacent in physical space are adjacent in index space are the monotonicity constraints (Boris, 1986),

$$x(i,j) \leq x(i+1,j) \text{ for } 1 \leq i \leq N_x - 1, \text{ all } j$$
$$y(i,j) \leq y(i,j+1) \text{ for } 1 \leq j \leq N_y - 1, \text{ all } i, \tag{1}$$

where N_x and N_y define the size of the particle array and x and y are the Cartesian coordinates, respectively. A system of particles that satisfies the monotonicity conditions is said to be in MLG order.

In the types of simulations considered here, the positions of the particles change constantly, leading to violation of Equation (1). The MLG order can be restored by swapping data stored in adjacent indices until the monotonicity constraints of equation (1) are satisfied. The data swapping is done locally. This means, for instance, when particles move so that they are not of MLG order, their MLG indices and the data describing these particles are exchanged, or "swapped," until MLG order is ensured. Figure 3 shows the resorting process for a 4×4 MLG after a convection time interval Δt_g. This resorting process results in a grid which automatically adapts to the continually changing local number densities of the gas.

The MLG subdivides the $N_x \times N_y$ array of simulated particles into $n_x \times n_y$ templates, or blocks of nearest-neighbor particles. If $n_x = n_y$, the templates are square in index space, but not necessarily in physical space. Figure 4 shows an example of a nearest-neighbor template that has a population of 5×5 particles. When particles within an MLG template

6

are allowed to interact, the template becomes analogous to the grid cell in conventional DSMC applications.

Macroscopic properties are computed or "sampled" at the template's center-of-mass and depend on the template area. In conventional DSMC. the size of the grid cells are fixed. In DSMC-MLG, however, the continual change in the size of the templates requires continually updating of the template areas. The area of each template is computed by a very simple and fast routine. Assuming that the N_b boundary particles are labeled as $P_1, P_2, ..., P_{N_b}$ in a counterclockwise order, the template area A_t is given by

$$A_t = \frac{1}{2} \sum_{j=1}^{N_b} (x_j y_{j+1} - x_{j+1} y_j), \tag{2}$$

where x_j and y_j are the coordinates of particle P_j, and $x_{N_b+1} = x_1$, $y_{N_b+1} = y_1$. Calculating the template areas in this way does not account for the area between the template. To remedy this, each template is assigned to its own area a fraction of the area that is not accounted for (Cybyk et al., 1995). As a result, the sum of all corrected template areas then equals the area of the entire computational domain.

2.3 Stochastic Grid Restructuring

For a given system of particles, there are many possible MLGs that satisfy the monotonicity conditions. This is best illustrated by the example in Figure 5 (Oran and Boris, 1987). Here, for the same set of 16 particles, three of many possible grids are shown, all satisfying the monotonicity criteria. As a result, the quality of these MLGs can vary significantly. The MLG obtained by normal swapping of particle data described above may not be good enough, while better MLGs often exist for the same system of particles.

It is possible to find a high-quality MLG for a given spatial distribution of particles by using Stochastic Grid Restructuring (SGR) (Sinkovits et al., 1993). When this method is implemented in the DSMC-MLG, it is possible to obtain an optimal MLG for the problem considered. The SGR consists of three steps:

7

- The positions of the particles are temporarily and randomly perturbed by a displacement $(\delta x, \delta y)$, where $-x_{disp} \leq \delta x \leq x_{disp}$ and $-y_{disp} \leq \delta y \leq y_{disp}$. During this procedure, the unperturbed positions are retained.

- The MLG swapping procedures are applied to the perturbed particle positions until monotonicity conditions are satisfied.

- With the MLG for the perturbed positions as the starting point, the MLG swapping procedures are applied to the unperturbed particle positions until monotonicity conditions are satisfied.

The quantities x_{disp} and y_{disp} can be chosen independently, and their magnitudes greatly influence the final MLG. Several SGR iterations may be needed during a simulation timestep to improve the MLG. Figure 6 illustrates an example of MLG improvements using SGR. In Figure 6a, the MLG for a system of 6×6 particles without using SGR is shown. The MLGs in Figures 6b and c are obtained with one and two SGR iterations, respectively.

2.4 Parallelization of DSMC-MLG

The DSMC-MLG parallelization method used here is a two-level approach (Oh et al., 1996b). The first level maps particles to an array of processors, and the second level maps templates to an array of processors. These arrays are of different sizes; there are many more particles than templates. This two-level approach allows efficient use of computer storage memory by moving the data at the particle-array level to a much smaller array at the template level, thus reducing computational memory requirements.

The flowchart for the parallelized DSMC-MLG algorithm is shown in Figure 7. The shaded and striped blocks refer to the steps parallelized at the particle level and template level, respectively. Particle-level parallelization was performed for DSMC-MLG processes that involve computations and communications at the particle level only. These were the initialization, convection, MLG resorting, and SGR processes. Of these, the first two steps

8

were the simplest, involving no interprocessor communications. For example, in the convection step, all particles are moved simultaneously with their appropriate velocities with one single instruction. In this step, some, but not all, of the particles interact with the boundaries. In this case, the parallelization was implemented by selecting only those particles that interact with the boundaries, performing the interactions in parallel, then updating their velocities and positions. Although this process leads to a load balancing problem, the effect on the overall computing time is minor (Oh et al., 1996b).

MLG resorting and Stochastic Grid Restructuring were also performed at the particle level. In DSMC-MLG applications, the particles move only a small distance during each timestep, and thus are only slightly out of MLG order. The entire process of resorting into MLG therefore requires only nearest-neighbor communication rather than global communication. This is ideal, particularly on Connection Machine architecture, for the bubble sort algorithm, which compares values of nearest-neighbors of an array on all processors at the same time.

The template area (or cell volume for a three-dimensional application), center of mass, and other properties are evaluated at the template level for all templates simultaneously. The collision process is also parallelized at the template level.

2.5   Code Validation

The current code has been validated by comparing the results obtained to conventional DSMC computations by Bird for the Rayleigh problem (Cybyk et al., 1995), the theoretical oblique shock angles for the low-Knudsen-number limit in hypersonic flows (Oh et al., 1996b; Oh et al., 1996a), and the theoretical Mott-Smith ratio of the mean free path to the shock thickness for a monotonic gas (Oh et al., 1996a).

Computational speed and the DSMC-MLG have been extensively described in the literature. Cybyk et al. (Cybyk et al., 1995) showed that serial DSMC-MLG is indeed slower than the conventional DSMC approach in standard simplified test problems. However, there

9

are significant advantages even in the serial form for more complex problems, such as those that require grid adaptivity to resolve high gradients or moving bodies. In the DSMC-MLG, there is, by definition, always enough particles in each MLG cell to maintain optimal collision statistics (Cybyk et al., 1995). Oh et al. (Oh et al., 1996b) showed very high parallel efficiencies and speed ups of two orders of magnitude or more compared to the serial DSMC-MLG, and the efficiency increases dramatically as the number of particles increases. DSMC-MLG computations are scalable and allow simulations of millions of particles for engineering computation.

2.6 Inflow-Outflow Boundary Condition

In the original applications of the DSMC-MLG, the inflow-outflow boundary condition was applied in index space. The result was that the downstream boundary could move and became distorted in physical space during the simulation (Cybyk; 1994). However, because it is most useful to fix the length of the system *a priori*, a new inflow-outflow boundary condition was developed for this application (Nguyen, 1995). The procedures for maintaining this constant-length boundary are illustrated in Figure 8, which show that the boundary condition is applied in physical space rather than in index space. After the particles are moved for a timestep Δt_g, those particles which cross over a prescribed boundary are reintroduced at the inflow by resetting their velocities to freestream values and distributing them at random locations at the inflow boundary. As a result, the total number of simulated particles is kept constant for all times, the total molecular mass in the system is conserved, and the length of the system stays constant throught the simulation. Finally, the particles are resorted into MLG order. These procedures are repeated for every convection timestep.

3 GRID, RESOLUTION, AND CONVERGENCE STUDIES

Figure 9 illustrates the geometry and the boundary conditions for the channel-wedge flow, and Table 1 is a summary of the flow conditions. The computational domain consists of a rectangular channel, and a small freestream section upstream of the leading edges of the channel. A wedge, with half angle θ, is placed on the bottom surface of the channel downstream from the leading edge. The channel is filled with quiescent rarefied helium gas. For the conditions in Table 1, the Knudsen number, based on the channel height, is 0.184, which is in the transitional flow regime.

The flow is initialized at Mach 5 everywhere. The wall surfaces are kept at the freestream temperature and are modeled as fully diffused boundaries. The upper and lower boundaries of the freestream section ahead of the channel are specularly reflecting. Particles that move past the outflow boundary are reintroduced at the inflow with their properties reset to freestream conditions.

Initial simulated results showed what appeared to be a "blocked" flow, with a normal shock standing near the inlet of the channel (Cybyk, 1994). This phenomena in channel flow is also a common experimental problem. Now we initialize the calculation with molecular velocities that are a small amount (3%) above those that subsequently flow into the channel. This method is very similar to common experimental practices used to overcome choked flows that often occur in supersonic and hypersonic nozzles.

3.1 MLG Grid Generation Problem

The standard MLG sorting process does not take into account the presence of an obstacle in the flow field. As a result, in the vicinity of the obstacle, an MLG template could contain particles from both the front and back sides of the obstacle. Such a template crosses the solid boundaries in physical space, even though the ordering of the particles satisfies monotonicity conditions. This is illustrated in Figure 10, where templates cross the wedge boundaries,

11

and one of the centers of mass is inside the wedge and therefore outside of the computational domain.

Figure 11 shows the evolution of the grid obtained by connecting the centers-of-mass of the templates. The presence of a grid point inside the wedge corresponds to the presence of a "saddled" template, one that saddles the wedge. These templates have extra area inside the wedge, which in turn causes the total area of all the templates to be larger than the computational area. The macroscopic properties at the centers-of-mass of these templates are incorrectly predicted as a result of the extra area. In addition, the particles in front of and behind the wedge are possible collision partners, which would not occur in a real flow. Therefore, to predict the flow properties accurately, it is necessary to make the MLG conform to the geometry.

This problem is resolved by a combination of two techniques: 1) concentration of a large number of particles along the wedge surfaces initially, and 2) sorting locally in the x-direction first before applying MLG sorting. Figure 12 shows that the resulting MLGs better conform to the wedge initially, and continue to do so during the simulation. There is only one center-of-mass inside the top-right corner of the wedge. However, the extra area this template adds is very small, and the particles are prevented in any event from crossing the solid boundaries. Any effect on the final solution is thus negligible, and is reduced with increasing grid resolution.

This approach produced a reasonable grid for the channel-wedge geometry. It was also applied successfully on a converging-diverging nozzle configuration (Nguyen, 1995). For more complex geometries, however, it might not give satisfactory results, and other techniques should be used. In one approach, a large number of particles concentrated on a surface could be used to define the solid boundary and form templates. They would not be allowed to move during the convection step, but would be allowed to collide with gas particles during surface interactions. Such extensions are currently being developed.

12

3.2 Grid Optimization

In Figure 13a, the grid initially used for the simulation sometimes slopes in the direction opposite to the flow structures, especially in the region upstream of the wedge. This results in a high level of fluctuations in the solution (Nguyen, 1995; Nguyen et al., 1994). A better MLG would result in a smaller fluctuation level and smoother results.

Several parameters can be used as a measurement of the quality of an MLG. These include the average link lengths between nearest neighbors and the average of the normalized dot products of the vectors joining the nearest neighbors with the unit normals. The link lengths are defined as

$$x_{link}(i,j) = |\mathbf{r}(i+1,j) - \mathbf{r}(i,j)|,$$

$$y_{link}(i,j) = |\mathbf{r}(i,j+1) - \mathbf{r}(i,j)|,$$

where $\mathbf{r}$ is the vector joining the nearest neighbors. The dot products are defined as

$$x_{dp}(i,j) = \frac{x(i+1,j) - x(i,j)}{x_{link}(i,j)},$$

$$y_{dp}(i,j) = \frac{y(i,j+1) - y(i,j)}{y_{link}(i,j)},$$

For a well-structured MLG, the average link lengths, which indicate the average inter-particle distance, are minimized. The average dot products are a measure of the relative direction between the nearest-neighbor link and the unit normals, or the orthogonality of the MLG grid. For example, if a set of four particles is arranged such that each particle resides on the lattice of a square, both the x and y dot products equal unity. A well-structured MLG has the largest possible average dot products.

A series of simulations was performed to examine the effects of different MLGs on the qualities and convergence of the computed flow. A nondimensional SGR displacement parameter, δ, is defined as

$$\delta = \frac{y_{disp}}{\Delta r}, \tag{3}$$

13

where Δr is the averaged template size. Five different values of δ (0.0, 0.5, 1.0, 2.0, and 4.0) were considered for the same grid resolution of 1504 templates (51,144 particles). Figure 13 shows the MLGs of the steady-state solutions obtained after 2000 timesteps. There is essentially no difference in the computing time of the simulations with and without the SGR. Once the SGR is used, the slope of the y grid reverses direction and is along the direction of flow structures (Figures 13b-e). The higher the value of δ, the more orthogonal the MLG.

The average link lengths, $\bar{x}_{link}$ and $\bar{y}_{link}$, are shown in Figure 14 as a function of the number of timesteps for all five cases. The values of $\bar{x}_{link}$ remain fairly constant during the simulation, and are approximately the same for all cases. The values of $\bar{y}_{link}$ fluctuate widely for the case without the SGR. However, with the SGR, $\bar{y}_{link}$ stays fairly constant with time. When $\delta = 2.0$, $\bar{y}_{link}$ is smallest, indicating that the average inter-particle distances are minimized.

The average dot products, $\bar{x}_{dp}$ and $\bar{y}_{dp}$, are shown in Figure 15 as a function of the number of timesteps. The average x dot products do not vary much. However, the average y dot products fluctuate widely without the SGR and remain essentially constant after the first few hundred timesteps for the other cases. Again, the MLG with $\delta = 2.0$ has the highest dot products and this results in the most orthogonal grid. These results are consistent with those for the average link lengths.

Since without the SGR, $\bar{y}_{link}$ and $\bar{y}_{dp}$ fluctuate widely, even after 2000 timesteps, the flow field has high level of statistical scattering, and is unfit for time-averaging. An optimal MLG appears to be the case where $\delta = 2.0$. However, it is unclear which grid gives the best solution for this problem since grid orthogonality is not required in these calculations. When $\delta = 0.5$, the MLG is highly adapted to the local number density of the flow. As δ increases, the orthogonality of the MLG increases, but it appears to conform less to the flow structure. An answer was found in the density contours in Figure 16 that compares the solutions of the highest quality MLG ($\delta = 2.0$) to the MLG most closely resembling the flow ($\delta = 0.5$). The flow fields were obtained by averaging 500 timesteps after the steady state was reached

after 2000 timesteps. Even though the results appear somewhat similar, a closer comparison show that for $\delta = 0.5$, the solution is better resolved, especially in the regions of the oblique shocks and their interaction at the channel centerline. Figure 17 shows that the density and temperature along the centerline of the channel are indeed very similar, except that the $\delta = 0.5$ case shows somewhat higher values of density in the shock-interaction region. The analysis of the flow field solution, presented in a later section, is for the $\delta = 0.5$ case.

3.3 Grid Resolution Study

A series of simulations of the channel-wedge problem was performed to study the sensitivity of the results to the number of MLG templates. Table 2 gives the properties of four different grids, with the number of templates ranging from 900 to 1800 and the number of simulated particles ranging from 32,400 to 64,800. In all of these cases, the SGR parameter δ is 2.0. The analysis could also be performed for $\delta = 0.5$, the most adaptive grid case. However, as seen in the previous section, results from the two cases are essentially the same, and therefore no significant effect on the analysis should be expected.

The grids for the four cases are shown in Figure 18 and the corresponding density contours are shown in Figure 19. The flow features obtained using the coarsest grid are not nearly as well resolved as those using 1504 and 1800 templates, which are very comparable. Figures 20 show the density distributions along the bottom and top surfaces of the channel. The results are comparable for all cases except the coarsest resolution. In particular, the differences between the 1504- and 1800-template cases are small, indicating grid-independence of the solution. Because a simulation on the 1504-template grid requires 35% less computing time than that on the 1800-template grid, the 1504-template grid is used for further studies.

3.4 Time-Averaging and Convergence

Due to the high ratio of actual to simulated molecules, there are large statistical fluctuations which must be greatly reduced to obtain a meaningful solution. This is be accomplished by time-averaging the solution once the steady state is established. Using the 1504-template

15

grid with $\delta = 0.5$, the flow reaches steady state after about 1000 timesteps. The simulation was then continued for a few hundred additional timesteps before time-averaging was started.

Figure 21 shows the density contours averaged over 40, 100, 300, and 500 timesteps beyond steady state. This is equivalent to averaging the solution over 40, 100, 300, and 500 independent ensembles, respectively. As the number of averaged timesteps (or ensembles) increases, the statistical fluctuations decrease. The results for the 300 and 500-timestep averagings are practically the same, indicating convergence.

Since the location and size of the MLG templates may change with time, it is interesting to consider whether the grid moves, and how much, during the time-averaging process. The calculations showed that at approximately 700 timesteps into the pre-averaged solutions, the grid no longer changed significantly. This is in agreement with the results described in Figures 14 and 15, which show the properties of the MLG — the averaged link lengths and dot products — remain constant with time after the few hundred initial timesteps. The MLGs taken at various sampling times, shown in Figure 22, are basically identical.

Figure 23 compares the density along the top and bottom surfaces of the channel for time-averaging stages of 40, 300, and 500 timesteps. The distributions are essentially the same, with the 40-timestep case showing more fluctuations.

4 ANALYSIS OF THE FLOW FIELD

4.1 Flow Features and Surface Properties

Figure 24 shows the converged solution, represented by density, temperature, pressure, and Mach number contours, for the 1504-template grid with $\delta = 0.5$. The flow field is similar to that in Figure 1, only now all of the flow structures are very diffused. However, it is still possible to identify many features.

The density contours in Figure 24a show the boundary-layer growth along the solid surfaces. The thickness of the boundary layers increases as the flow moves downstream. Near the outflow boundary, the flow expands as it leaves the channel, causing the boundary-layer thickness to decrease. The temperature contours in Figure 24b show the temperature of the gas in the core of the channel is much higher than that near the walls, which are held at a constant temperature of 273 K. As a supersonic flow expands through a rarefraction fan, the density, temperature, and pressure of the gas decrease. This effect is seen in the region immediately downstream of the trailing edge of the wedge in Figures 24a — c.

The pressure contours in Figure 24c show two oblique shocks emanating from the upper and lower leading edges of the channel and intersecting at about 10 cm downstream of the leading edges. The oblique shock angle is $\sim 22°$. This was estimated by measuring the angle of the pressure contours at the leading edge of the channel. The pressure contours also show that there is a third oblique shock at an angle of $\sim 40°$ emanating from the leading edge of the wedge. All of these shock structures interact near the centerline of the channel above the wedge forebody in a way similar to that shown in Figure 1. In the upper-half of the channel, a refracted shock interacts with the boundary layer near the upper wall and reflects downstream. In the lower-half of the channel, a weaker refracted shock merges with the rarefraction region that was caused by the supersonic expansion of the flow around the sharp corner of the trailing edge of the wedge. The flow then eventually turns parallel to the wall to form a very diffuse viscous layer downstream. In a continuum flow as in Figure 1, this layer would be a reattachment shock. The adverse pressure gradient (Figure 24c) across this

reattachment region causes the boundary layer to separate, and a reverse flow is developed just behind the trailing edge of the wedge. The pressure reaches a local maximum at the bottom wall near $x = 33$ cm as the flow crosses the reattachment layer. The Mach contours in Figure 24d show a supersonic core flow between the subsonic boundary layers and expansion near the outflow boundary.

Figures 25 shows the density, pressure, temperature, and magnitude of velocity along the top and bottom solid surfaces of the channel. Along the bottom surface, at about $x = 5$ cm, the pressure rises sharply across the leading-edge shock and increases significantly along the wedge surface due to the presence of the second oblique shock. Just ahead of the wedge trailing edge, the pressure drops across the rarefraction region as the flow expands, then increases again as the boundary layer develops. Along the top surface, the pressure increases across the leading-edge shock in the same manner as along the bottom surface. The pressure then rises markedly at about $x = 15$ cm due to the interactions between the boundary layer and the refracted shock.

Figure 25c shows the temperature of the gas adjacent to the walls. From this we see that the temperature jump is about four times the wall temperature near the leading edge and decreases rapidly further downstream. The magnitude of velocity in Figure 25d is what is called the velocity slip along the walls. At the entrance to the channel, the slip velocity is high because the density is low. As the boundary layer develops downstream, the density increases and the slip velocity drops sharply to near zero. A small increase in the slip velocity near the exit plane, $x = 40$ cm, indicates that the flow expands as it leaves the channel.

The development of the viscous boundary layers is shown in Figure 26 by the velocity profiles at various locations along the x-axis. At the leading edge of the channel, the boundary layers begin to form, and they grow as the flow moves downstream. The velocities are negative at the wall for 20 cm $< x <$ 22 cm, indicating a reverse flow.

The development of the thermal boundary layers is shown in Figure 27 by the temperature profiles at various locations along the x-axis. Compared to the velocity profiles in Figure 26,

the temperature profiles are not as symmetric, reflecting different shock strengths due to the presence of the wedge. The temperature profiles also show the temperature jump near the walls.

4.2   Comparisons of Flow Properties

For an inviscid flow, with no boundary layers and infinitely thin walls, the leading-edge shocks degenerate to Mach waves. For $M_\infty = 5$ flow, the angle of such a Mach wave would be 11.54°, which is much smaller than the 22° of the shock angle calculated in this study, indicating the displacement effect of the boundary layer. The boundary layer grows rapidly in the leading edge region and acts as an effective body that deflects the incoming streamlines upward. As a result, the shock at the leading edge is nearly normal to the surface of the channel. Across this shock at the surface, p_2/p_1 is approximately 5. This is much smaller than the pressure rise of 29 across a continuum normal shock, and is a consequence of the low density conditions.

When a high-velocity flow is slowed by the presence of a surface boundary, the viscous dissipation in the boundary layer transforms the high kinetic energy of the molecules into internal energy of the gas. This causes a large increase in the gas temperature, which in turn causes the viscosity coefficient to increase. The net effect is that the boundary layer becomes thicker and grows more rapidly than it would for lower-speed flows at the same Reynolds number (Anderson, 1989). This boundary layer causes a major displacement effect on the outer inviscid flow. In turn, the changes in the inviscid flow affect the properties of the boundary layer. This phenomenon is called viscous interaction.

In continuum flow, the viscous interaction near the leading edge may be described by the similarity parameter $\overline{\chi}$, defined as (Anderson, 1989)

$$\overline{\chi} = \frac{M_\infty^{\,3}}{\sqrt{Re_x}}\,\sqrt{C}. \tag{4}$$

The quantity C is the Chapman-Rubesin parameter and is defined as

$$C = \frac{\rho_w \mu_w}{\rho_\infty \mu_\infty},\tag{5}$$

where the subscript w indicates wall properties. In the continuum flow regime, $\overline{\chi}$ dictates the induced pressure along the surface of a flat plate. For a cold-wall flat plate, the induced pressure for a weak interaction is (Hayes and Probstein, 1959)

$$\frac{p}{p_\infty} = 1 + 0.078\overline{\chi}.\tag{6}$$

In low-density flows, the pressure interaction near the leading edge should be less pronounced than that in the continuum flow due to slip effects. Figure 28 compares the pressure near the leading edge of the top surface of the channel with that calculated by Equation (6). The pressure in the low-density case is consistently smaller than that in the continuum approximation. Also, the pressure drop in the vicinity of the leading edge (the region indicated by the smaller values of $1/(A\overline{\chi})$ in the abscissa) is due to the fact that the leading-edge shock diffuses out over the leading edge of the channel.

Figure 29 compares the results from the present study to those obtained from a DSMC calculation (Chpoun et al., 1993) for a near-continuum, $M_\infty = 4$ flow over a 20° compression corner. Figure 29a shows the surface pressure distribution as a function of the nondimensionalized distance x/L_f, where L_f is 5 cm, the length of the flat section upstream of the leading edge of the wedge. Due to the higher freestream Mach number, the pressure in the present study is consistently higher than that from Chpoun et al.

Figure 29b compares the velocity distribution along the ramp surface. The more rarefied condition ($Kn = 0.184$) in the present work resulted in a more gradual slip in the velocity adjacent to the surface. In contrast, the near-continuum condition ($Kn = 0.0047$) in Chpoun et al. caused a much sharper decrease near the leading edge of the flat section.

4.3 Skin Friction and Heat Transfer

The skin friction on the walls of the channel is calculated by averaging the parallel momentum transfer of the molecules impinging on the surfaces. Let the parallel momentum of an incident

molecule be P_{inc}, and that of the same molecule after reflection be P_{refl}, such that

$$P_{inc} = m V_{\|_{inc}},$$

$$P_{refl} = m V_{\|_{refl}}, \tag{7}$$

where m is the mass of each molecule, and $V_\|$ is the component of velocity parallel to the surface. The total change in the parallel momentum of the molecule, $\Delta P_\|$, is given by

$$\Delta P_\| = P_{inc} - P_{refl}. \tag{8}$$

The skin friction, τ_w, on a small surface area, ΔA, over an incremental time, Δt_g, generated by the impinging molecules is

$$\tau_w = \frac{\sum \left(\Delta P_\| \right)}{\Delta A \Delta t_g}, \tag{9}$$

where the summation sign indicates the total contribution from all impinging molecules. During a DSMC calculation, the skin friction on the surfaces of the solid walls may be sampled at any time using Equation (9). The heat flux, q_w, at the walls may be calculated in a similar manner by replacing the parallel momentum with the energy of the impinging molecule.

The results are presented in terms of the dimensionless skin friction coefficient, c_f, and the Stanton number, st, which are given by (Anderson, 1989)

$$c_f = \frac{\tau_w}{\frac{1}{2} \rho_e V_e^2}, \tag{10}$$

and

$$st = \frac{q_w}{\rho_e V_e (h_{aw} - h_w)}, \tag{11}$$

where the subscript e refers to conditions at the edge of the boundary layer, h_w is the enthalpy at the wall, and h_{aw} is the enthalpy if the wall is assumed to be adiabatic. The adiabatic wall enthalpy is evaluated in terms of the recovery factor, r, by (Anderson, 1989)

$$h_{aw} = h_e + r \frac{V_e^2}{2}. \tag{12}$$

The recovery factor is taken equal to $\sqrt{Pr}$, where Pr is the Prandtl number (Anderson, 1989). For helium, $Pr = 0.7$ (White, 1974). In this study, the freestream conditions are assumed at the edge of the boundary layers.

The skin friction and heat transfer to the top and bottom surfaces of the channel are shown in Figure 30. Along the bottom surface, the value of c_f is highest near the leading edge where the high-velocity molecules are slowed down substantially by the solid boundaries. The skin friction coefficient decreases downstream, then increases along the wedge surface, reaching a local maximum near the end of the wedge. Behind the trailing edge of the wedge, c_f becomes negative in the recirculation region. Futher downstream, c_f stays fairly constant, with a slight increase near the exit plane where the flow expands.

Along the top surface, c_f peaks near the entrance plane and decreases downstream. A local maximum of c_f occurs near $x = 25$ cm as a result of the interaction between the refracted shock and the boundary layer adjacent to the top wall. The distributions of st are similar to those of c_f. The Stanton number is positive everywhere, including the recirculating region, indicating the transfer of heat from the flow to the walls. Figure 30 represents an average of 1000 timesteps. These figures indicate that the skin friction and heat transfer require more timestep averaging than the state properties to obtain the same level of fluctuations.

The results along the top wall agree well with those obtained by a DSMC calculation of a hypersonic flow along a flat plate (Moss et al., 1991). In their results, both the skin friction and heat transfer peak near the leading edge and decrease downstream. The peak c_f in Moss et al. (1991) is approximately 0.07 compared to 0.056 for the top wall in this study. The peak st in Moss et al. (1991) is 0.02, whereas it is about 0.03 for the top wall. The quantitative differences are due to the different freestream and wall temperature conditions.

In incompressible flow theory, the Stanton number and the skin friction coefficient along a laminar flat plate are related by the Reynolds analogy (Anderson, 1989),

$$st = c_f \frac{1}{2} \, Pr^{-\frac{2}{3}}. \tag{13}$$

Even though, the flow is hypersonic in this study, it is interesting to see how much the results

in Figure 30 deviate from the above relation. Figure 31 compares two distributions of the Stanton number: one from the DSMC simulations (Figure 30), and the other calculated by substituting the computed c_f into the Reynolds analogy of Equation (13). In Figure 31a, the two distributions of st along the top wall compare very well, except for the region near the interaction between the refracted shock and the boundary layer. In Figure 31b, the two distributions are about the same along the flat section of the bottom wall ahead of the wedge. Downstream of this section, however, the Reynolds analogy values deviate from the DSMC values due to the presence of the wedge. The results in these figures show that the Reynolds analogy might still be applicable for high-M, high-Kn flow along flat plates with the freestream and wall temperature conditions similar to those in this study. Other freestream and wall conditions must be investigated before the Reynolds analogy can be generalized.

5 CONCLUSION

Simulations of a rarefied, high-Kn flow of helium gas through a channel with a wedge have been performed using the combined DSMC-MLG algorithm. These simulations were used both to describe the flow features and their interactions under rarefied conditions, and to develop and test a new approach to the DSMC algorithm. Because this work had a fluid dynamic as well as algorithmic objective, an extensive series of computations was performed for a single physical system.

The resulting computations present a highly resolved picture of a flow field that was compared qualitatively to what would be expected in a continuum flow. Where possible, the results were compared quantitatively to theoretical analysis and computations. Since the flow is so rarefied, the flow features, such as oblique shocks, rarefraction fan, and boundary layers, and their interactions are diffuse. The pressure jump across the leading-edge shock at the surface is considerably less than that for a continuum normal shock. Comparisons to hypersonic weak viscous interaction theory for continuum flow show that the pressure interaction near the leading edge is less pronounced under rarefied conditions. Downstream of the trailing edge of the wedge, the reattachment shock that is typical in a continuum flow degenerates into a very diffuse viscous layer.

The effects of low-density conditions are also shown in the slip in velocity and temperature of the gas adjacent to the solid surfaces. The slip velocity is highest at the entrance of the channel where the density is low, and decreases more gradually than that for a near-continuum conditions in the work of Chpoun et al. (1993). Similarly, the temperature jump peaks near the leading edges reaching approximately four times the wall temperature, and then decreases further downstream as the boundary layers develop.

The skin friction and heat transfer calculations show that peak shear force and thermal loading occur near the leading edges of the channel. The effects of the wedge on the flow field are shown in local maxima of skin friction coefficient and Stanton number distributions on the bottom wall. In addition, viscous interactions between the refracted shock and the

boundary layer near the top wall result in an increase in skin friction and heat transfer. These calculations compare fairly well with DSMC calculations on a flat plate by Moss et al. (1991). The Stanton number distribution along the top wall compare well with that calculated by the Reynolds analogy for incompressible boundary-layer flow, suggesting that the Reynolds analogy might be applicable for high-speed, rarefied flow along flat plates under conditions similar to those in this study. These results, along with the slip velocity and temperature jump data, provide a benchmark for testing phenomenological and theoretical models that attempt to extend the applicability of the NS equations to other flow regimes.

Another important aspect in this study is the development and implementation of a new inflow-outflow boundary condition. Previous applications of DSMC-MLG used an inflow-outflow boundary condition that causes the downstream boundary to move in physical space during the simulation. The new boundary condition effectively keeps the length of the the channel-wedge geometry constant throughout the simulation while conserving the total molecular mass in the system.

The MLG provides the DSMC with automatic grid adaptation according to local number density and gives correct collision rates everywhere in the flow field. The DSMC-MLG combination, when implemented on a massively parallel computer, is extremely efficient and allows simulations of very large numbers of particles. For the specific problem of the flow through a channel-wedge, a typical calculations of 65,000 particles took about 20 minutes or less to converge on the 256 node CM-5. There were a number of practical questions about using the DSMC-MLG that have now been resolved. This work has provided substantial insight into issues of the grid generation in the presence of an obstacle, the resolution required in terms of the number of simulated particles, the effects of grid structure on the solution and how to find an optimal grid, and what is required in terms of averaging the solution to eliminate the effects of statistical fluctuations.

Acknowledgment

References

Allen, M. P. and Tildesley, D. J. (1990). *Computer Simulations of Liquids*. Clarendon Press, Oxford.

Anderson, Jr., J. D. (1989). *Hypersonic and High Temperature Gas Dynamics*. McGraw-Hill, Inc., New York.

Beskok, A. and Karniadakis, G. E. (1994). Simulation of heat and momentum transfer in complex microgeometries. *Journal of Thermophysics and Heat Transfer*, 8(4):647–655.

Bhatnagar, P. L., Gross, E. P., and Krook, M. (1954). *Phys. Rev.*, 94:511.

Bird, G. A. (1963). Approach to translational equilbrium in a rigid sphere gas. *Phys. Fluids*, 6:1518–9.

Bird, G. A. (1976). *Molecular Gas Dynamics*. Clarendon Press, Oxford.

Bird, G. A. (1987). Nonequilibrium radiation during reentry at 10km/s. *AIAA Paper no. 87-1543*.

Bird, G. A. (1989). Perception of numerical methods in rarefied gasdynamics. In *Progress in Astronautics and Aeronautics*. Vol. 118, edited by E. P. Muntz, AIAA, Washington, D.C.

Bird, G. A. (1990). Application of the direct simulation monte carlo method to the full shuttle geometry. *AIAA Paper no. 90-1692*.

Boris, J. P. (1986). A vectorized "near-neighbors" algorithm of order n using a monotonic logical grid. *Journal of Computational Physics*, 66:1–20.

Carlson, A. B. and Wilmoth, R. G. (1992). Shock interference prediction using direct simulation monte carlo. *AIAA Paper no. 92-0492*.

Chpoun, A., Lengrand, J. C., Cohen, L., and Heffner, K. S. (1993). Dsmc numerical investigation of rarefied compression corner flow. *AIAA Paper no. 93-3096*.

Cybyk, B. Z. (1994). *Combining the Monotonic Lagrangian Grid with Direct Simulation Monte Carlo; a New Approach for Low-Density Flows*. PhD thesis, Aerospace Engineering Dept., University of Maryland.

Cybyk, B. Z., Oran, E. S., Boris, J. P., and Anderson, J. D. (1995). Combining the monotonic lagrangian grid with a direct simulation monte carlo model. *Journal of Computational Physics*, 122:323–334.

Dagum, L. (1991). Three dimensional direct particle simulation on the connection machine. *AIAA Paper no. 91-1365*.

Dogra, V. K., Moss, J. N., Wilmoth, R. G., Taylor, J. C., and Hassan, H. A. (1994). Effects of chemistry on blunt body wake structure. *AIAA Paper no. 94-0352*.

Furlani, T. R. and Lordi, J. A. (1989). A comparison of parallel algorithms for the direct simulation monte carlo method ii: Application to exhaust plume flowfields. *AIAA Paper no. 89-1167*.

Goldstein, D. and Sturtevant, B. (1989). Discrete velocity gasdynamics simulations in a parallel computing environment. *AIAA Paper no. 89-1668*.

Hayes, W. D. and Probstein, R. F. (1959). *Hypersonic Flow Theory*. Academic Press, New York.

Kogan, M. N. (1969). *Rarefied Gas Dynamics*. Plenum Press, Translated from Russian by Leon Trilling, New York.

Moss, J. N. (1986). Numerical simulations of rarefied reentry flows. *AAS 86-348*.

Moss, J. N. and Bird, G. A. (1984). Direct simulation of transitional flow for hypersonic re-entry conditions. *AIAA Paper no. 84-0223*.

Moss, J. N., Bird, G. A., and Dogra, V. K. (1988). Nonequilibrium thermal radiation for an aeroassist flight experiment vehicle. *AIAA Paper no. 88-0081*.

Moss, J. N., Price, J. M., and Chun, C. (1991). Hypersonic rarefied flow about a compression corner – dsmc simulation and experiment. *AIAA Paper no. 91-1313*.

Nanbu, K. (1982). Theoretical basis of the direct simulation monte carlo method. *Journal of the Physical Society of Japan*.

Nguyen, T. X. (1995). *Enhancements of the Parallelized DSMC-MLG Method for Applications to Complex Hypersonic Transitional-Regime Flows*. PhD thesis, Aerospace Engineering Dept., University of Maryland.

Nguyen, T. X., Oh, C. K., Saint-Martin-Tillet, X. N., Piana, J. V., and Oran, E. S. (1996). Knudsen-number effects in high-speed microchannel flows. In *Proceedings of the 20th International Symposium on Shock Waves*.

Nguyen, T. X., Oran, E. S., Anderson, J. D., Oh, C. K., Sinkovits, R. S., and Cybyk, B. Z. (1994). Hypersonic low-density flow computations using dsmc-mlg on massively parallel supercomputer.

Oguchi, H. (1963). Leading edge slip effects in rarefied hypersonic flow. In *Rarefied Gas Dynamics*. Supplement 2, Vol. II, edited by J. A. Laurmann, Academic Press, N.Y.

Oh, C. K., Oran, E. S., and Cybyk, B. Z. (1995). Microchannel flow computed with the dsmc-mlg. *AIAA Paper no. 95-2090*.

Oh, C. K., Oran, E. S., and Sinkovits, R. S. (1996a). Computations of high-speed, high-knudsen-number microchannel flows. *to appear in Physics of Fluids*.

Oh, C. K., Sinkovits, R. S., Cybyk, B. Z., Oran, E. S., and Boris, J. P. (1996b). Parallelization of dsmc combined with the monotonic lagrangian grid. *AIAA Journal*.

Oran, E. S. and Boris, J. P. (1987). *Numerical Simulation of Reactive Flow*. Elsevier Science Publishing.

Pan, Y. S. and Probstein, R. F. (1966). Rarefied flow transition at a leading edge. In *Fundamental Phenomena in Hypersonic Flow*. edited by J. G. Hall, Cornell University Press, Ithaca, N.Y.

Probstein, R. F. and Pan, Y. S. (1963). Shock structure and the leading edge problem. In *Rarefied Gas Dynamics*. Supplement 2, Vol. II, edited by J. A. Laurmann, Academic Press, N. Y.

Rault, D. F. G. (1992). *AIAA Paper no. 92-0306*.

Sinkovits, R. S., Boris, J. P., and Oran, E. S. (1993). A technique for regularizing the structure of a monotonic lagrangian grid. *Journal of Computational Physics*, 108:368-72.

Taylor, J. C., Moss, J. N., and Hassan, H. A. (1989). Study of hypersonic flow past sharp cones. *AIAA Paper no. 89-1713*.

White, F. M. (1974). *Viscous Fluid Flow*. McGraw-Hill, Inc.

Wilmoth, R. G. (1989). Direct simulation monte carlo analysis on parallel processors. *AIAA Paper no. 89-1666*.

Table 1: Flow conditions for the channel-wedge simulation.

Definition	Flow Condition Parameter	Value
length of channel	x_{max}	35 cm
height of channel	y_{max}	7.5 cm
wedge half-angle	θ	10°
freestream density	ρ_{ug}	2.0e-9 g/cm^3
freestream temperature	T_∞	273 K
freestream Mach number	M_∞	5
wall temperature	T_w	273 K
freestream mean free path	λ_{ug}	1.38 cm
Knudsen number	$Kn = \lambda_{ug}/y_{max}$	0.184
number of particles/template	N_t	6×6

Table 2: Computational parameters for the grid sensitivity study.

Number of Templates	Grid Size	Molecules per Template	Total Number of Simulated Molecules
900	75×12	6×6	32400
1200	80×15	6×6	43200
1504	94×16	6×6	54144
1800	100×18	6×6	64800
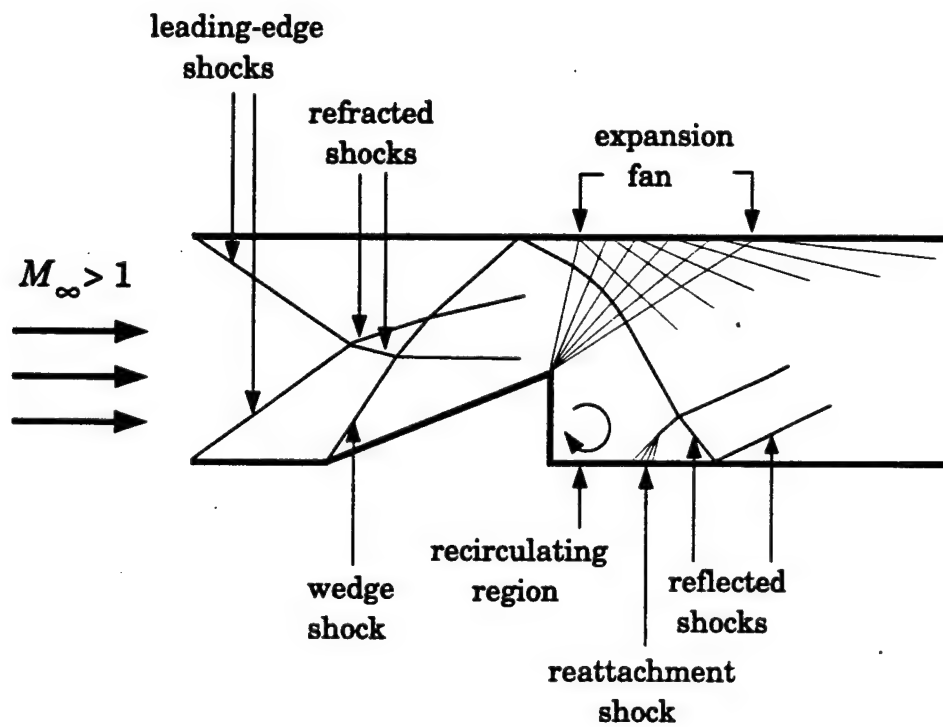
Figure 1: A typical continuum flow field in the channel-wedge geometry.
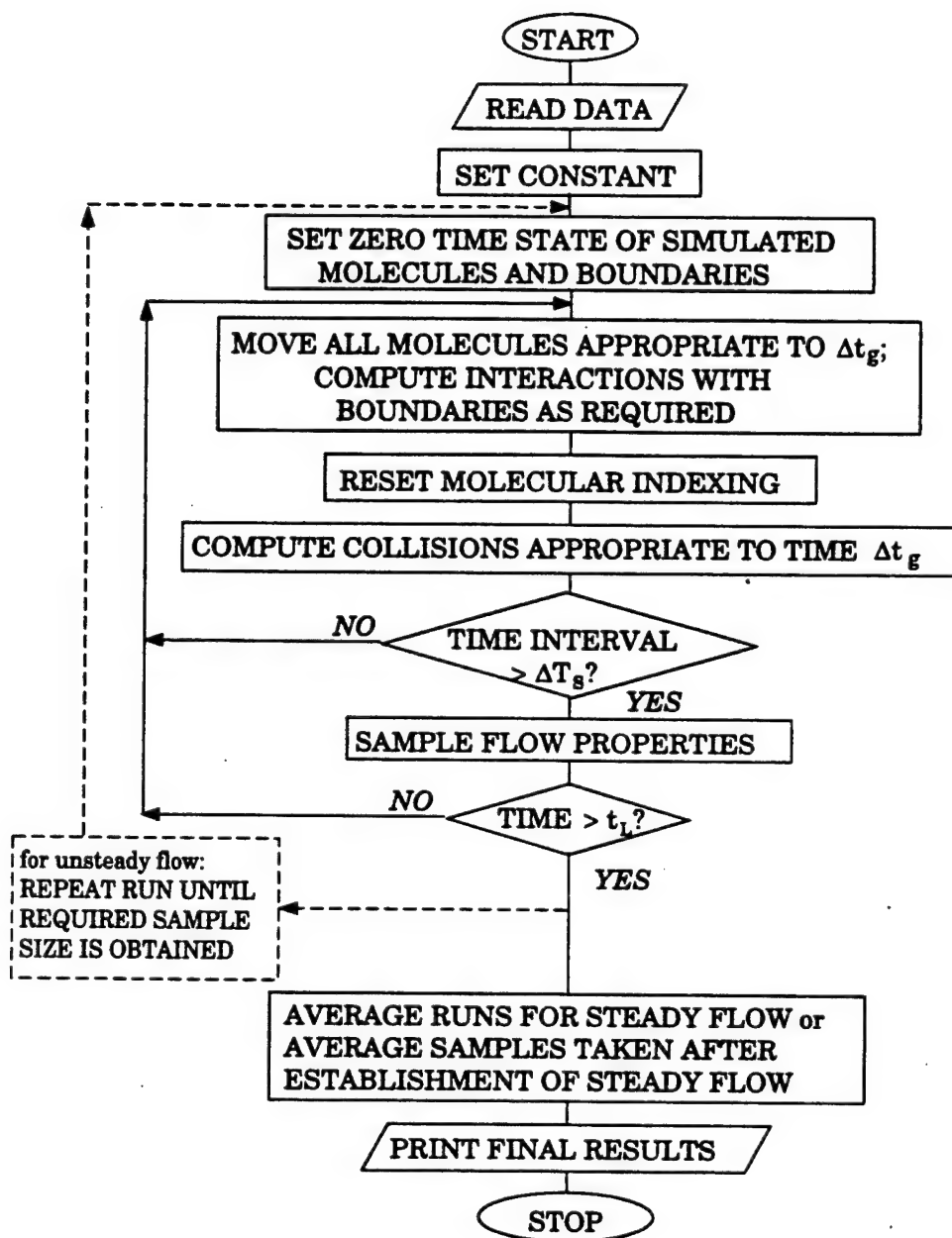
Figure 2: Flowchart for a conventional Direct Simulation Monte Carlo computation.

a) time t

b) time t + Δtg,
before resorting

c) time t + Δtg,
after resorting
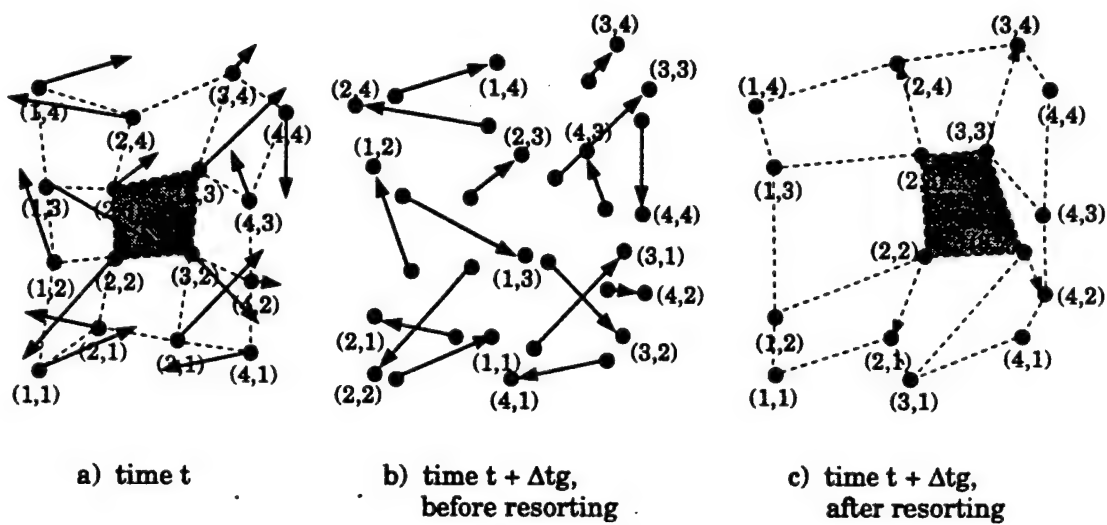
Figure 3: Example of an MLG resorting process.
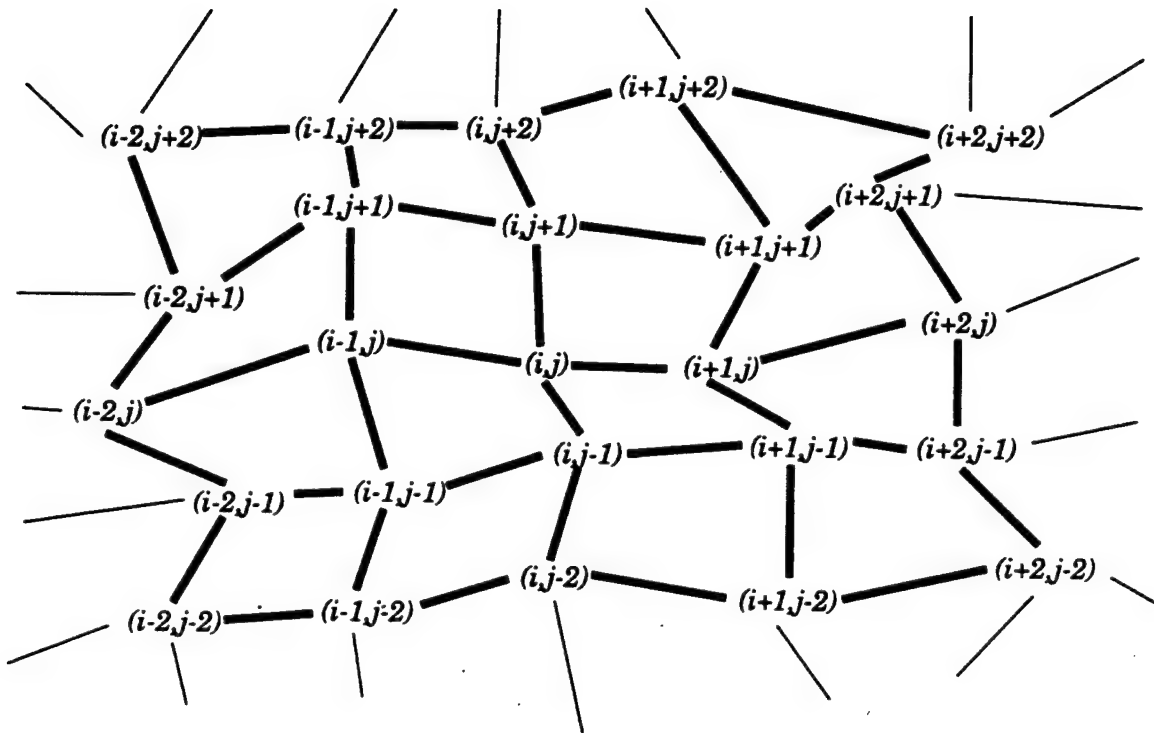
Figure 4: Example of a 5x5 template of nearest neighbors.
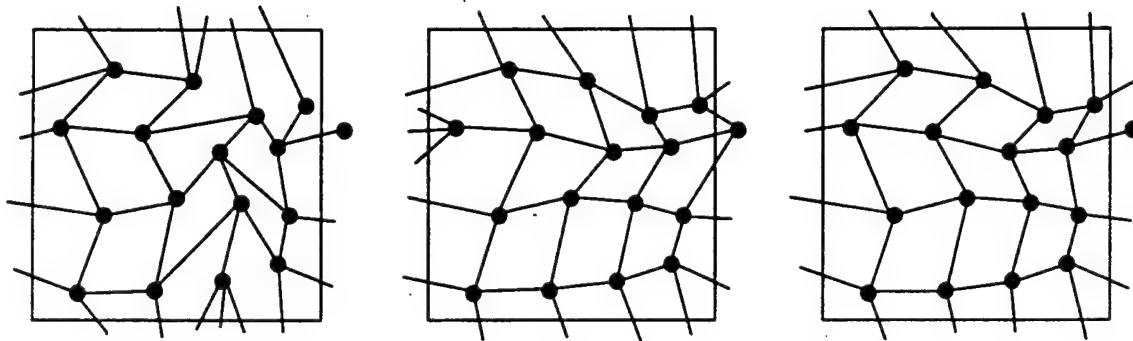
Figure 5: An example of three grids that are consistent with the same MLG monotonicity constraints [Oran and Boris, 1987]
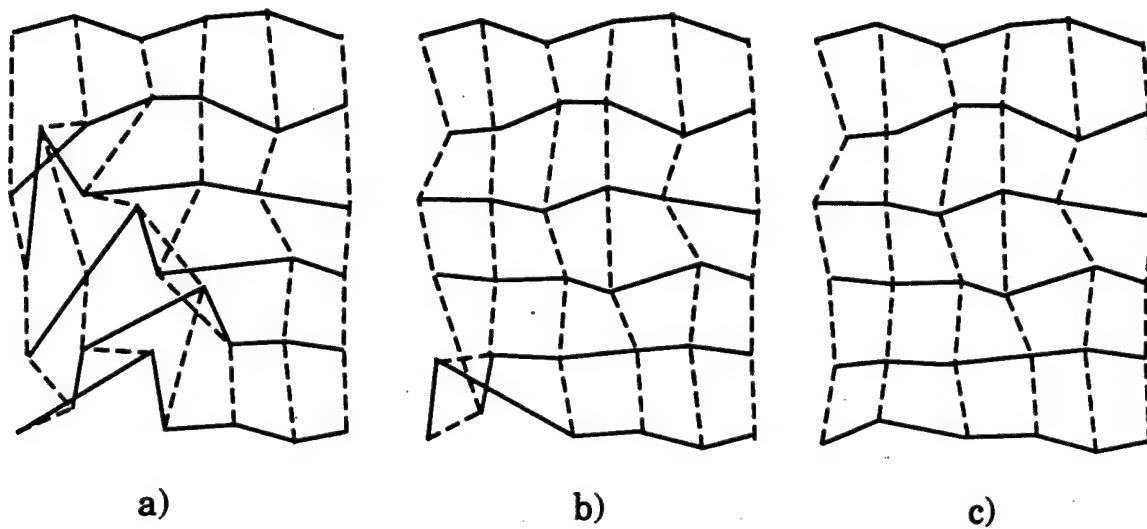
Figure 6: Example of MLGs for the same set of particle locations. a) Before applying SGR, b) after one SGR iteration, and c) after two SGR iterations [Sinkovits et al., 1993]
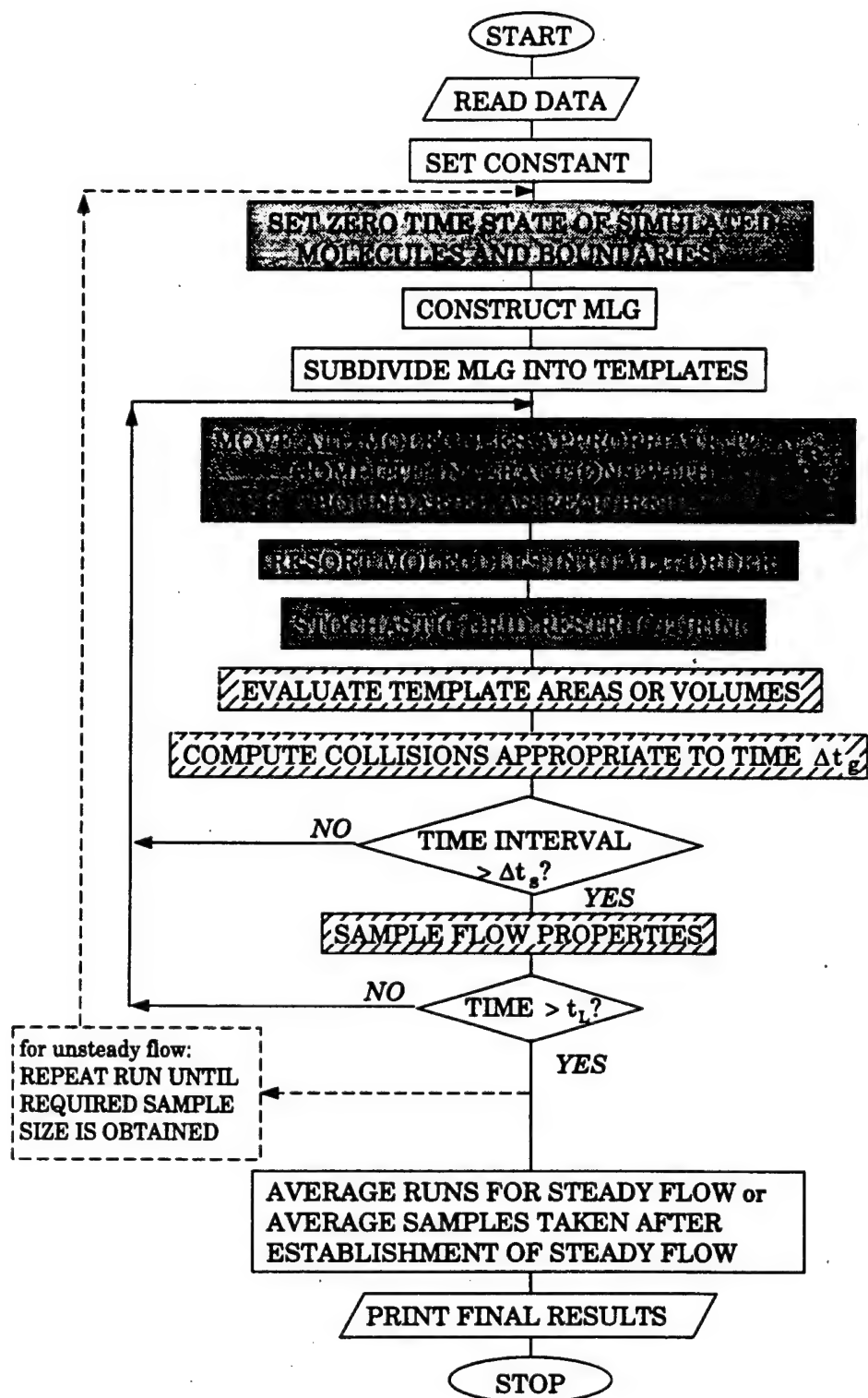
Figure 7: A flowchart of the parallelized DSMC-MLG algorithm [Oh et al., 1995].
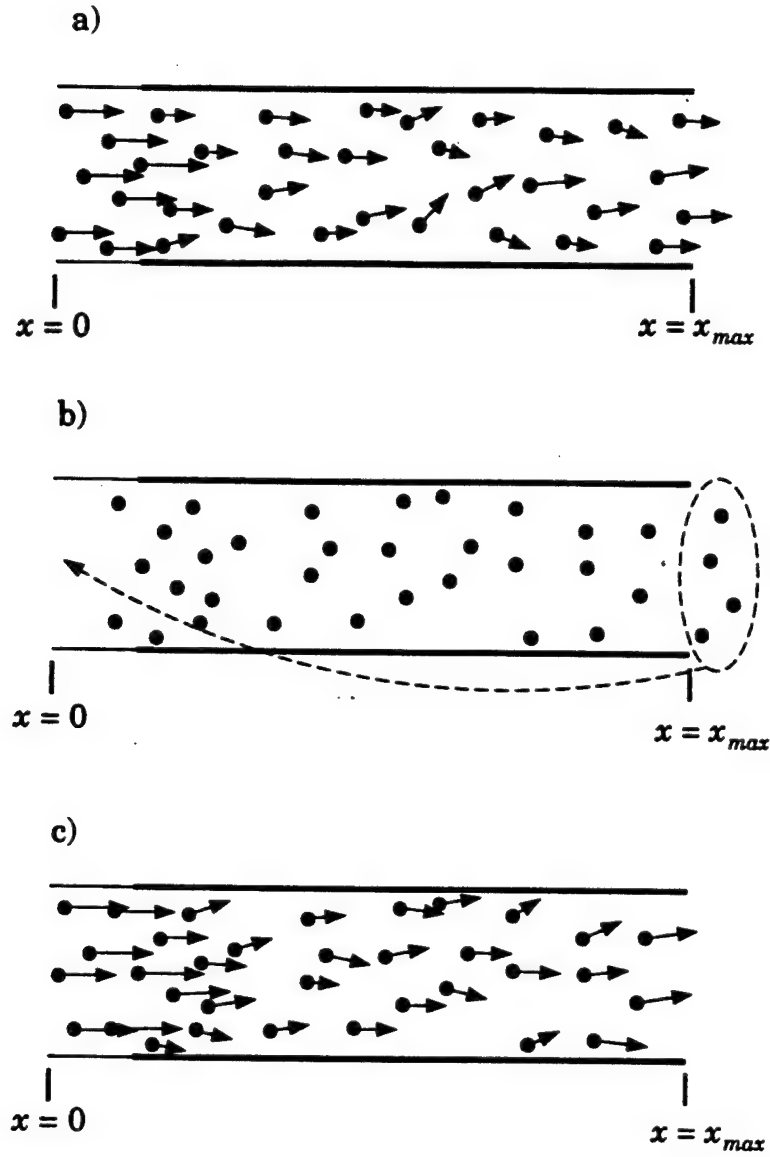
Figure 8: The procedures used in the constant-length boundary condition. a) The particles are move for a Δt_g, b) those that move past $x = x_{max}$ are re-introduced at the inflow, c) these particles are assigned freestream conditions.
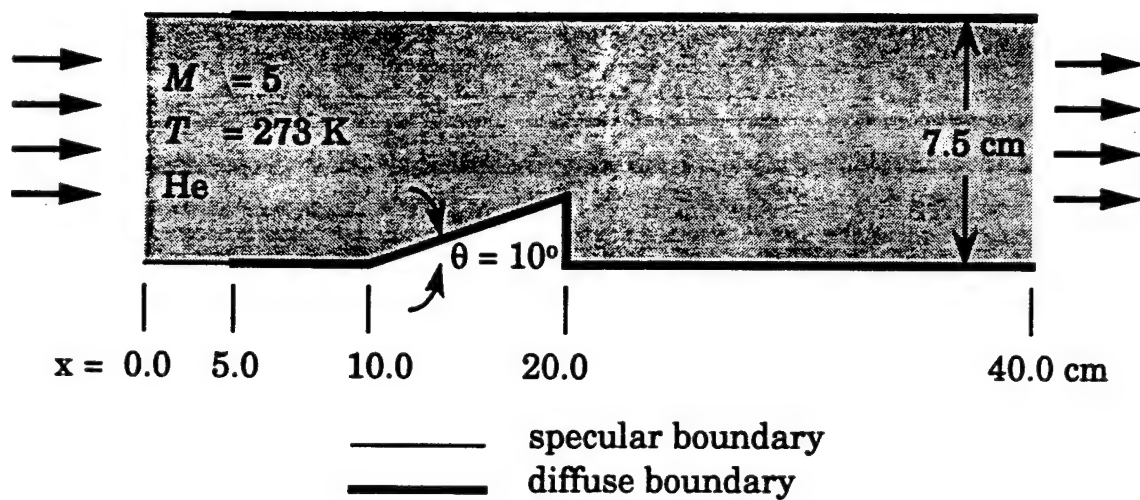
Figure 9: Schematic of the channel-wedge flow numerical experiment.
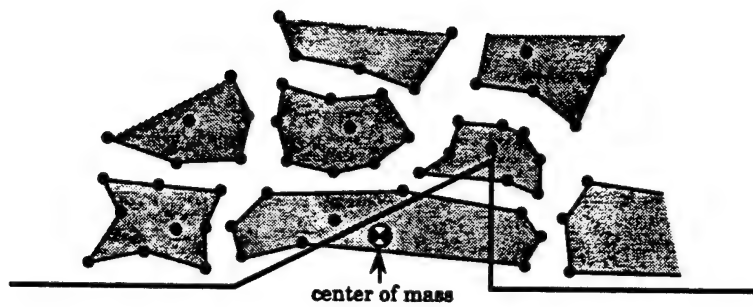
Figure 10: Schematic showing how templates may cross solid boundaries.
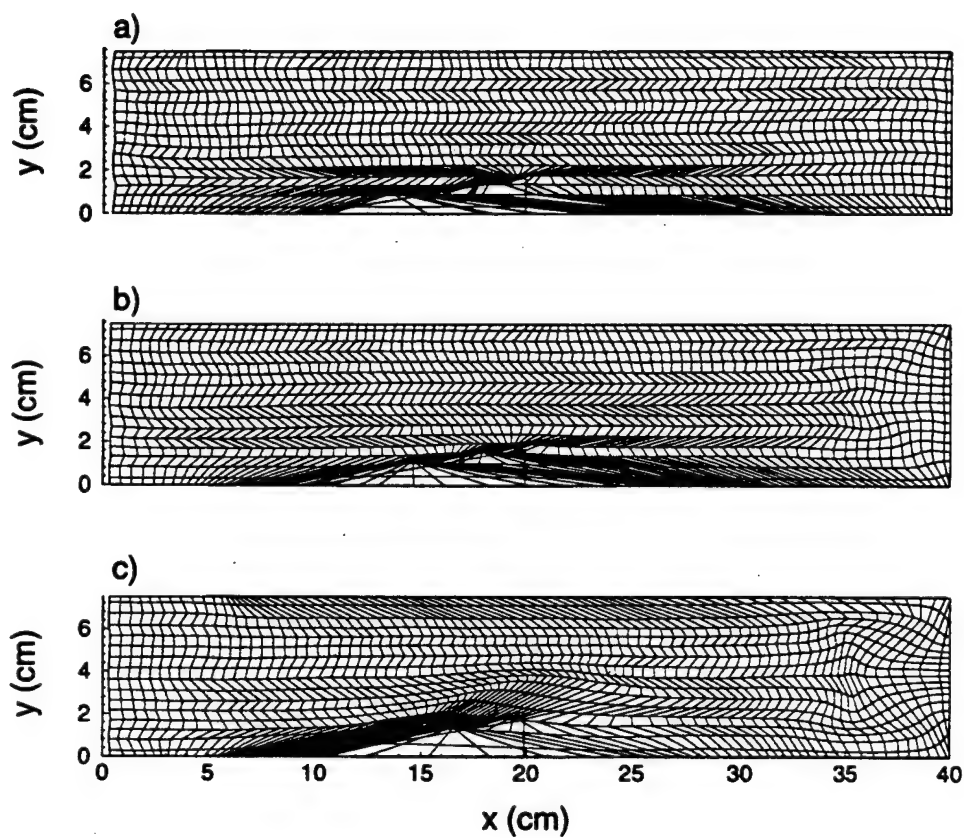
Figure 11: MLGs for the channel-wedge simulation. Grids do not conform to the geometry. a) Initial grid, b) after 50 timesteps, c) after 100 timesteps.
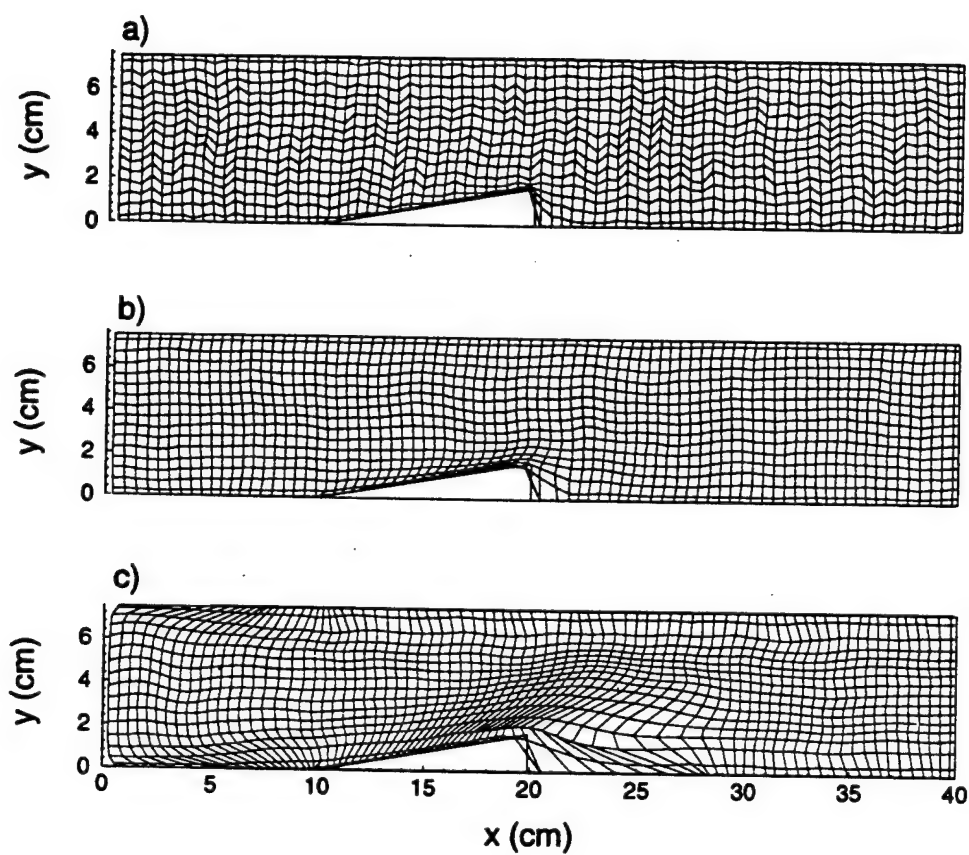
Figure 12: MLGs for the channel-wedge simulation. Grids conform to the geometry. a) Initial grid, b) after 50 timesteps, c) after 100 timesteps.
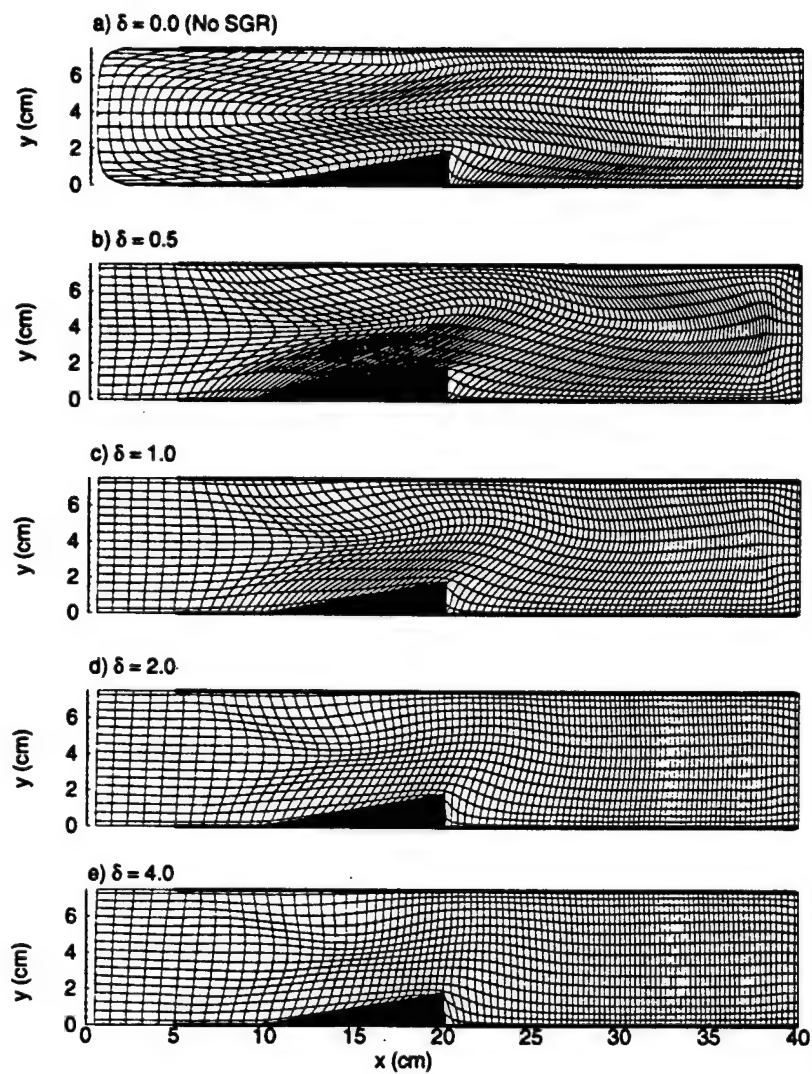
Figure 13: MLGs of the channel-wedge flow problem using SGR with five different δ values.
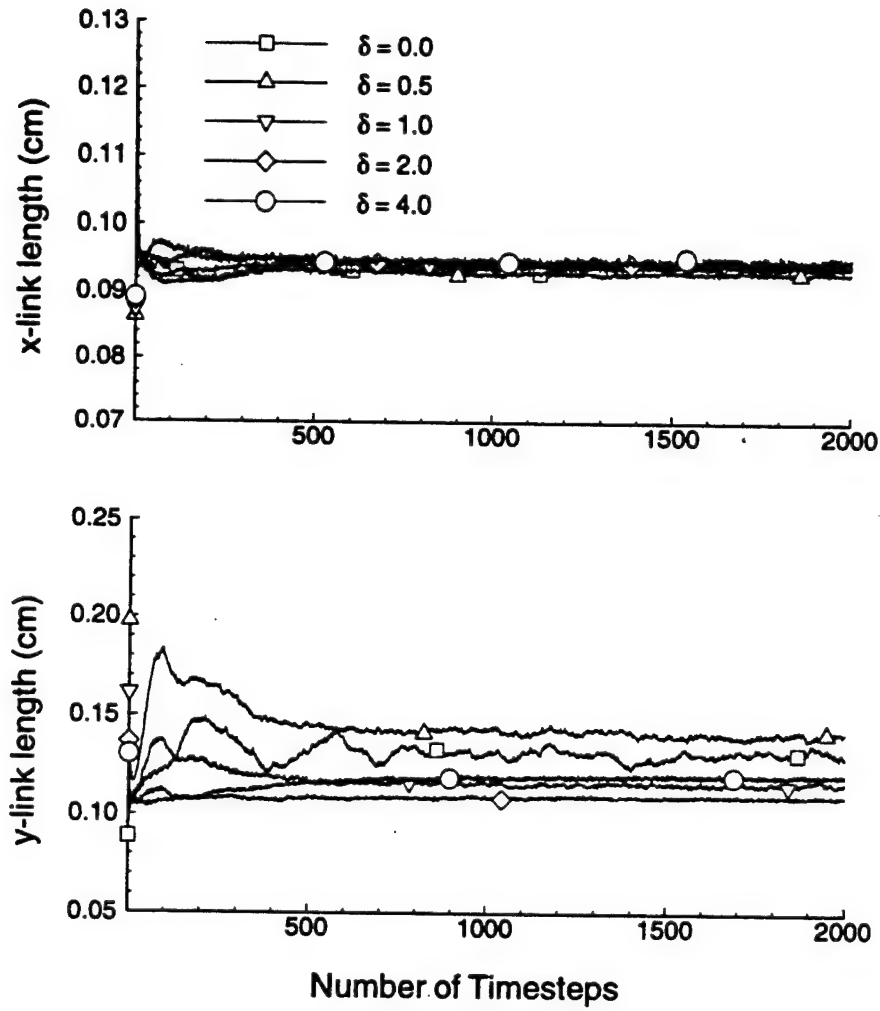
Figure 14: Average link lengths for the MLGs shown in Figure 13.
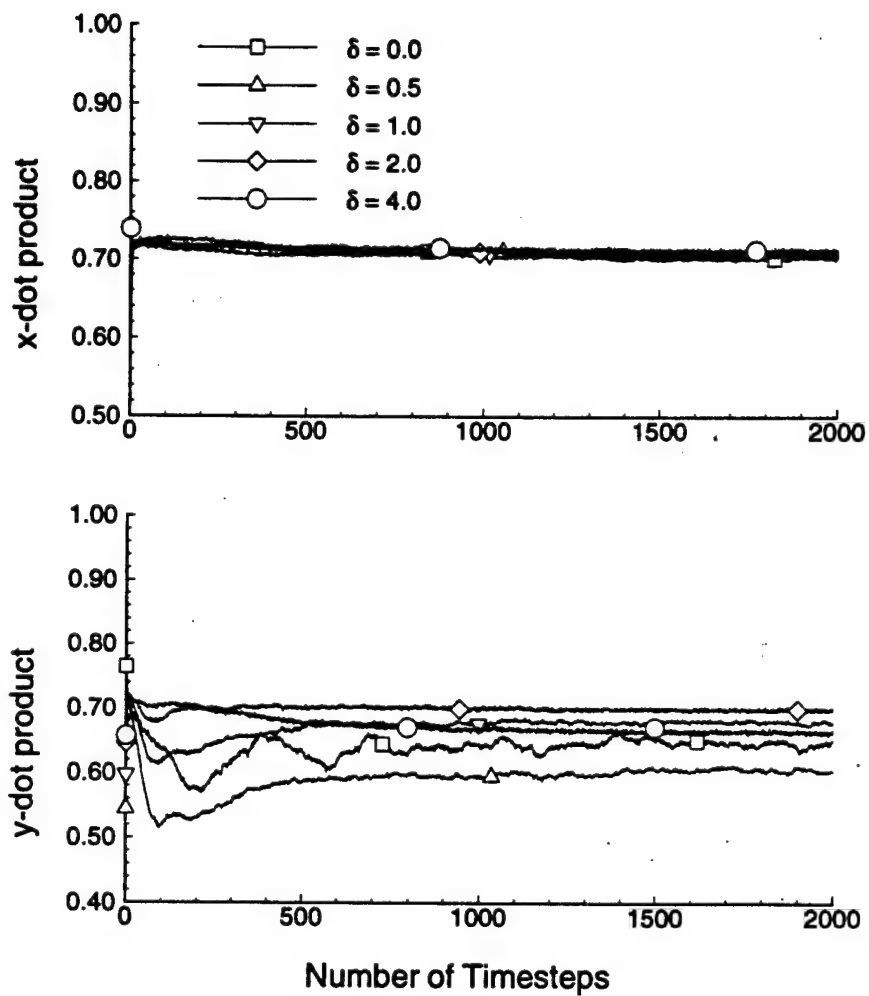
Figure 15: Average dot products for the MLGs shown in Figure 13.
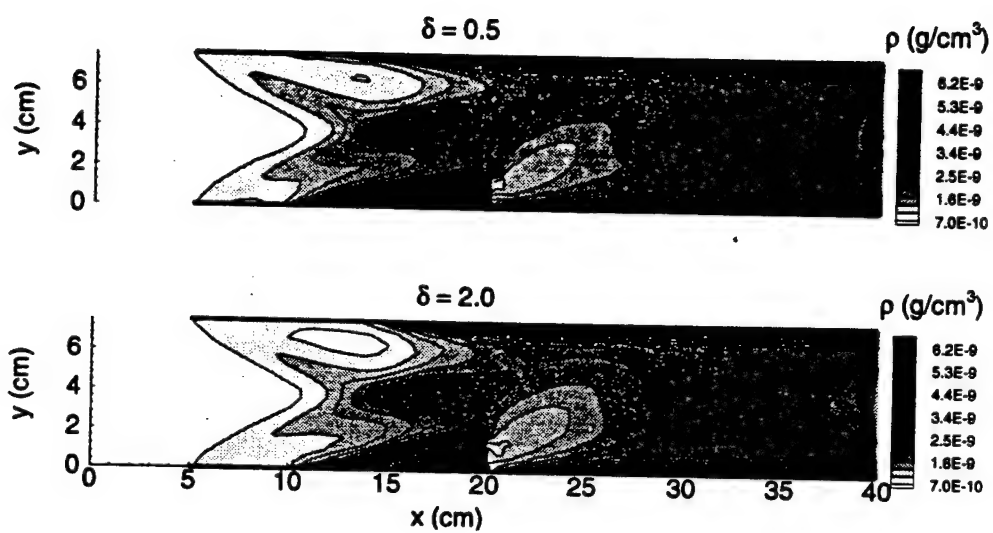
Figure 16: Comparsion of density contours of the channel-wedge flow field for different displacement parameters.
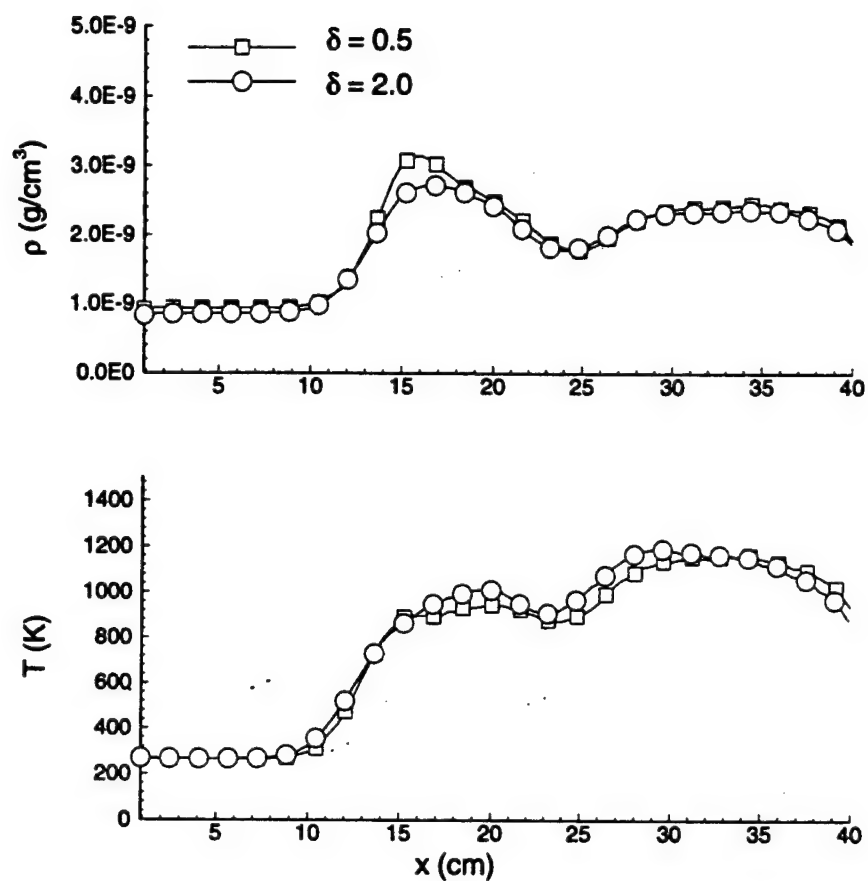
Figure 17: Comparsion of computed density and temperature distributions along the cen-
terline of the channel.
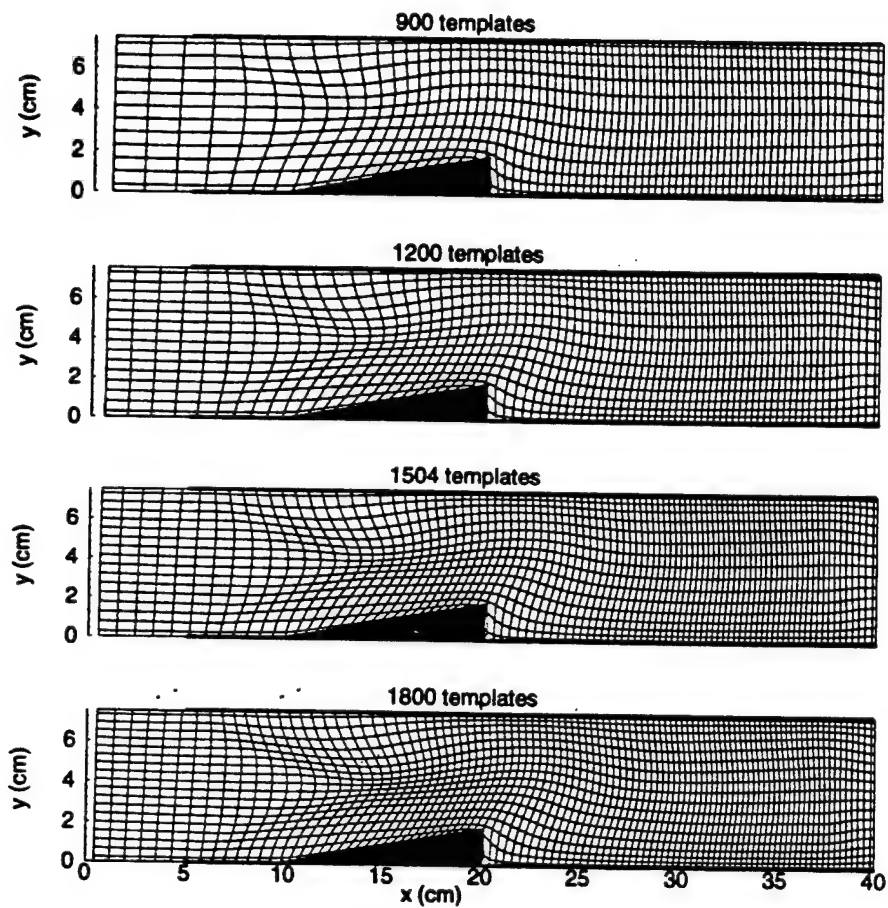
Figure 18: MLGs for the grid resolution study.
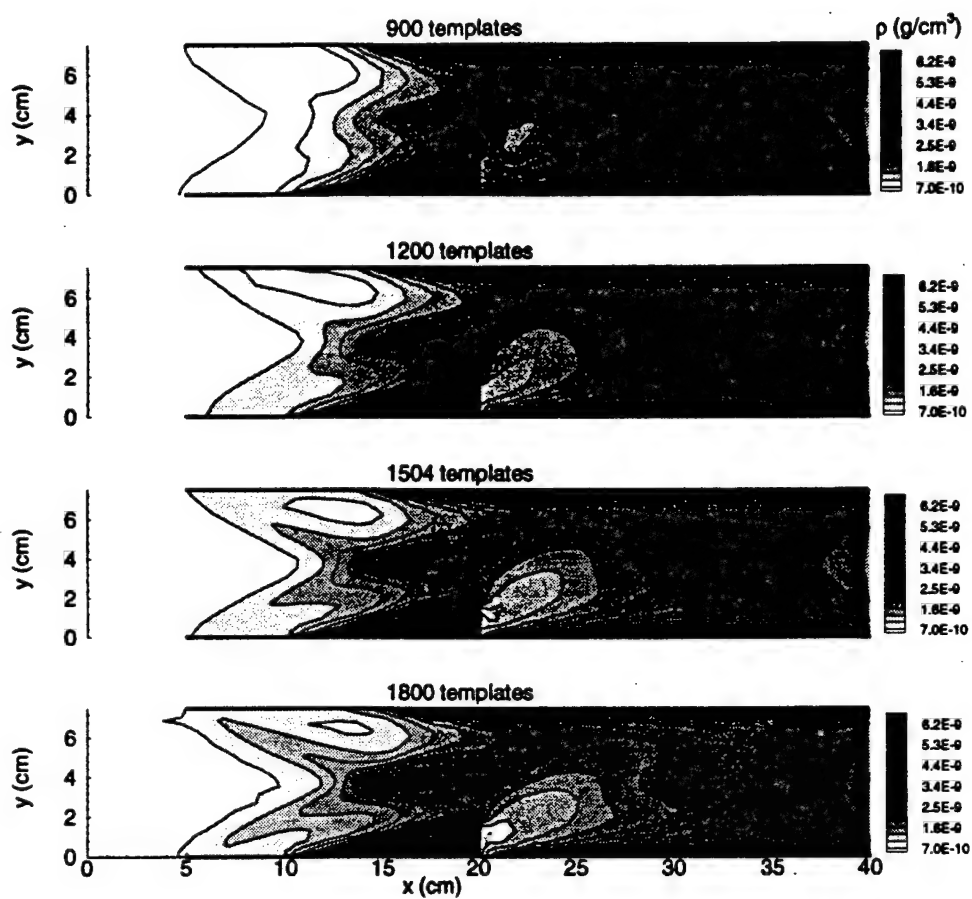
Figure 19: Density contours for the four grid resolutions.
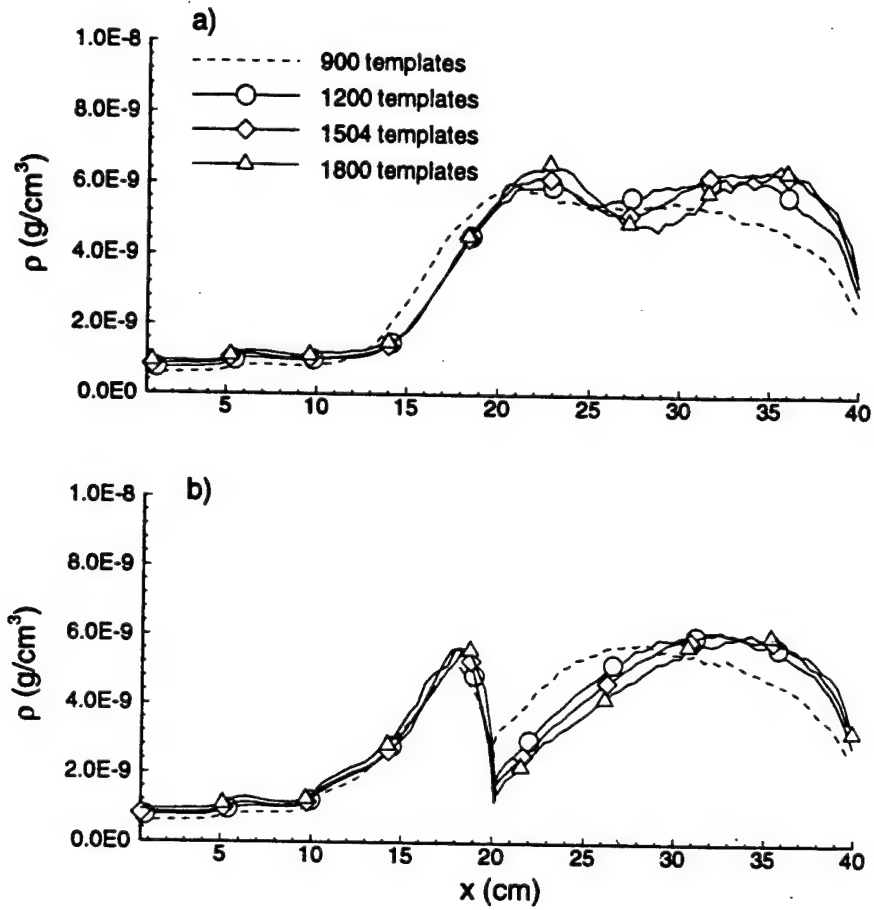
Figure 20: Comparison of density distributions for the four grid resolutions: a) top surface, b) bottom surface of the channel.
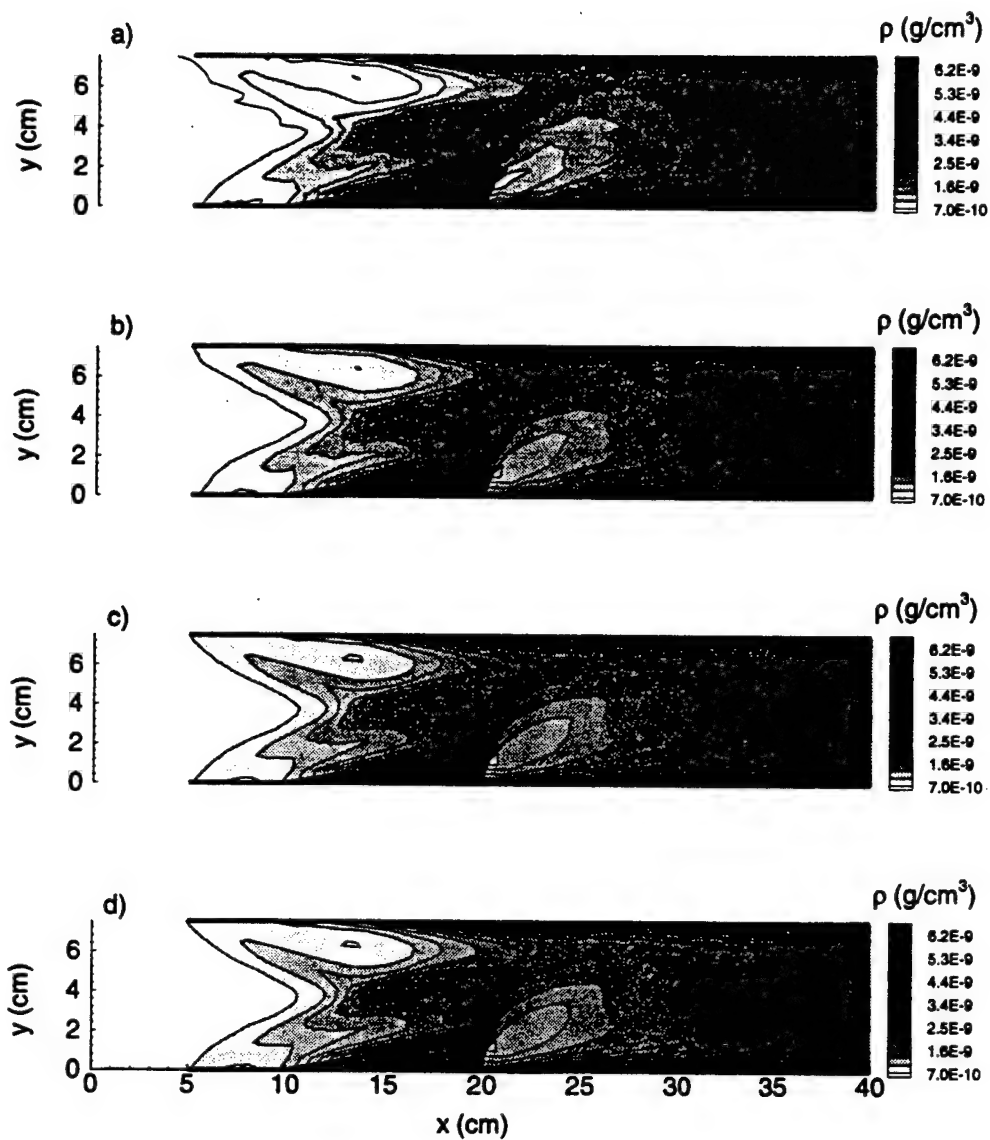
Figure 21: Flow field density contours for a) 40, b) 100, c) 300, and d) 500 time-averaging steps.
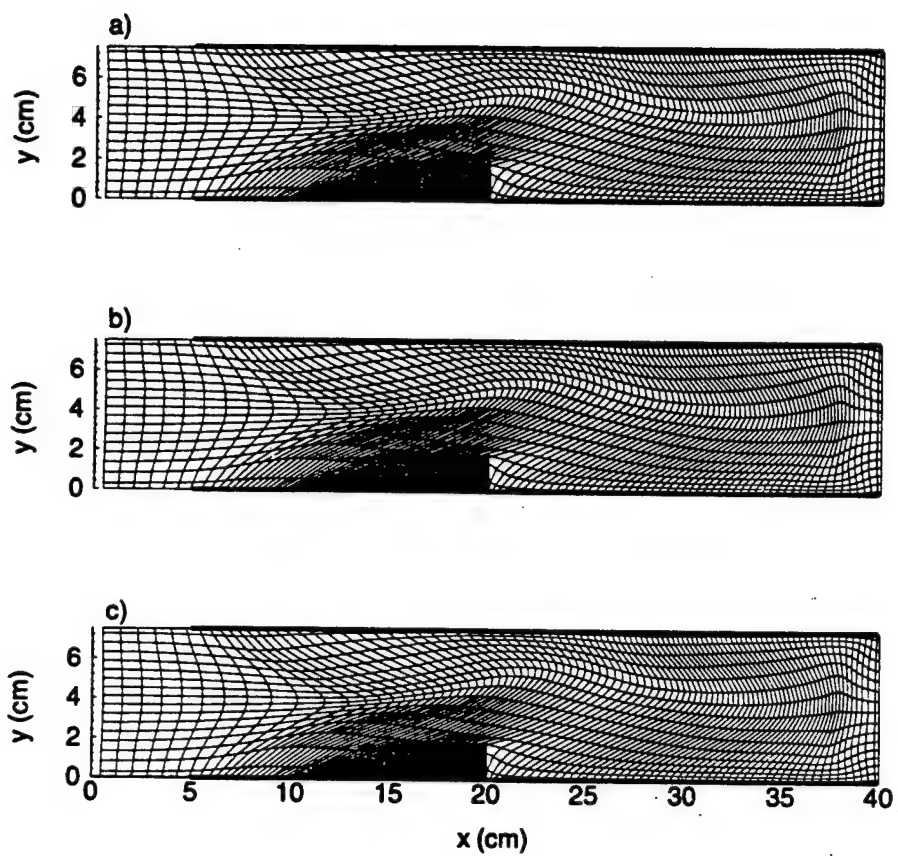
Figure 22: Comparison of 1504-template MLGs for a) 40, b) 100, and c) 500 time-averaging steps
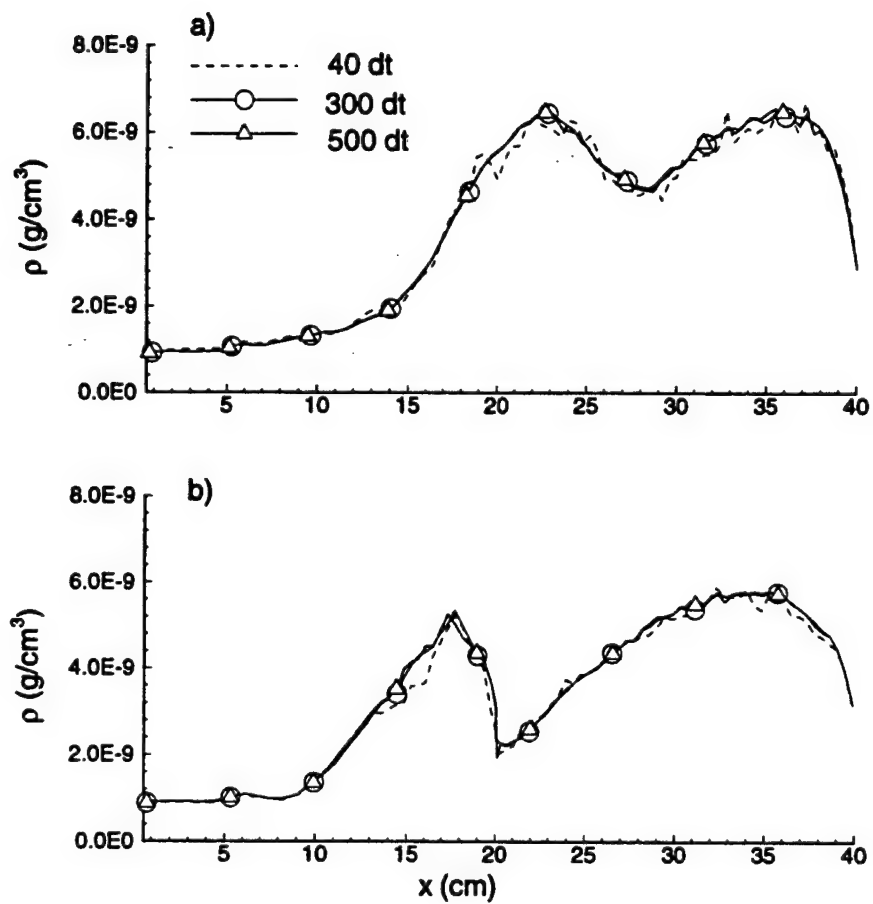
Figure 23: Comparison of density distributions for various time-averaging steps.
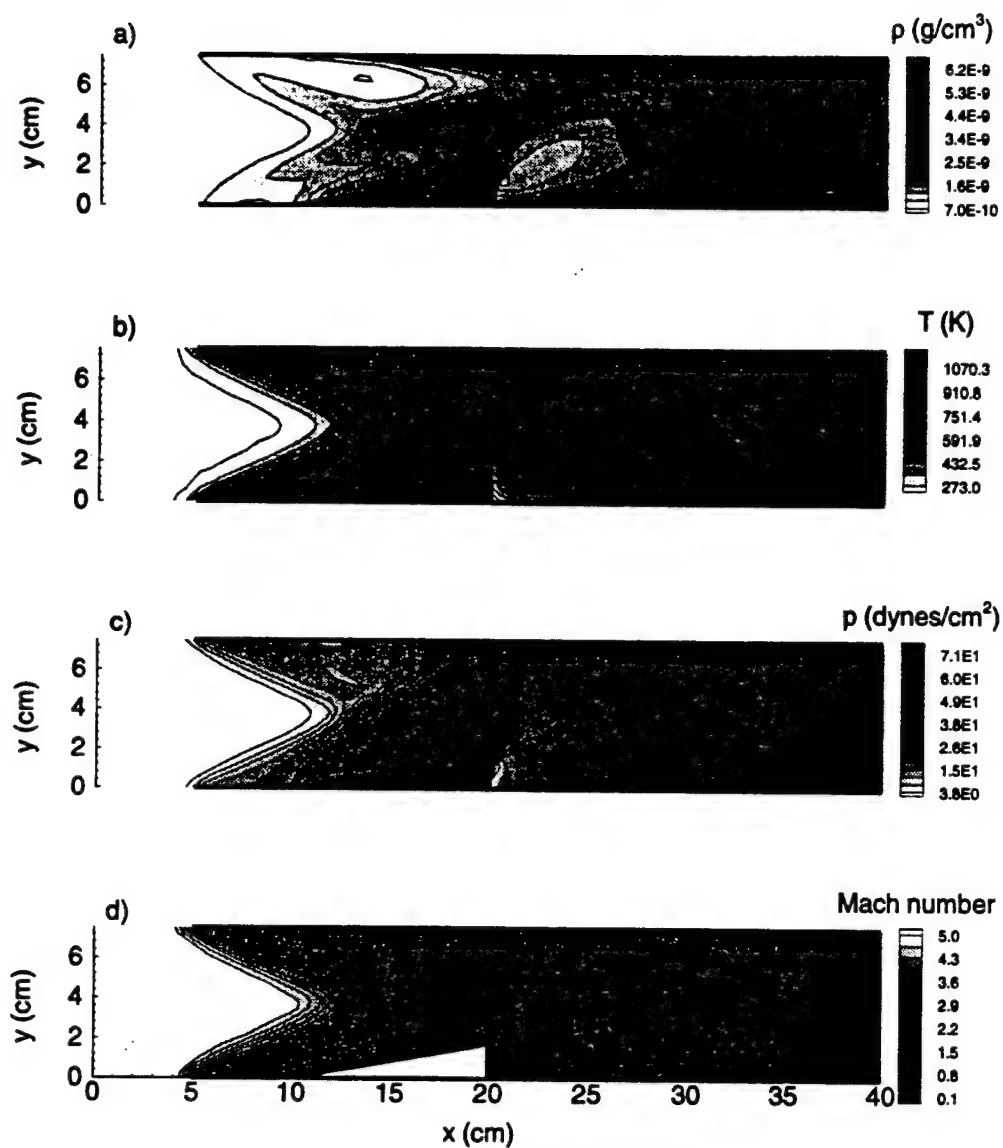
Figure 24: Converged solution of the channel-wedge simulation.
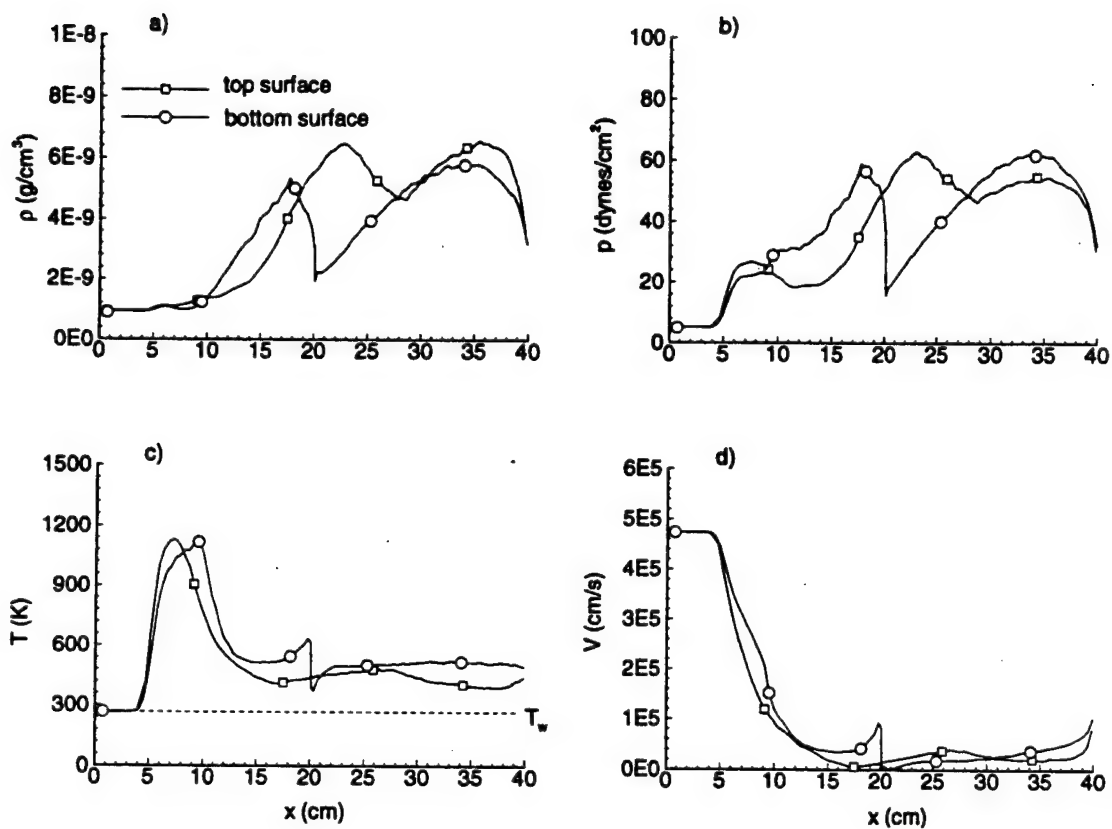
Figure 25: Macroscopic properties along the channel-wedge solid surfaces: a) density, b) pressure, c) temperature, d) magnitude of velocity.
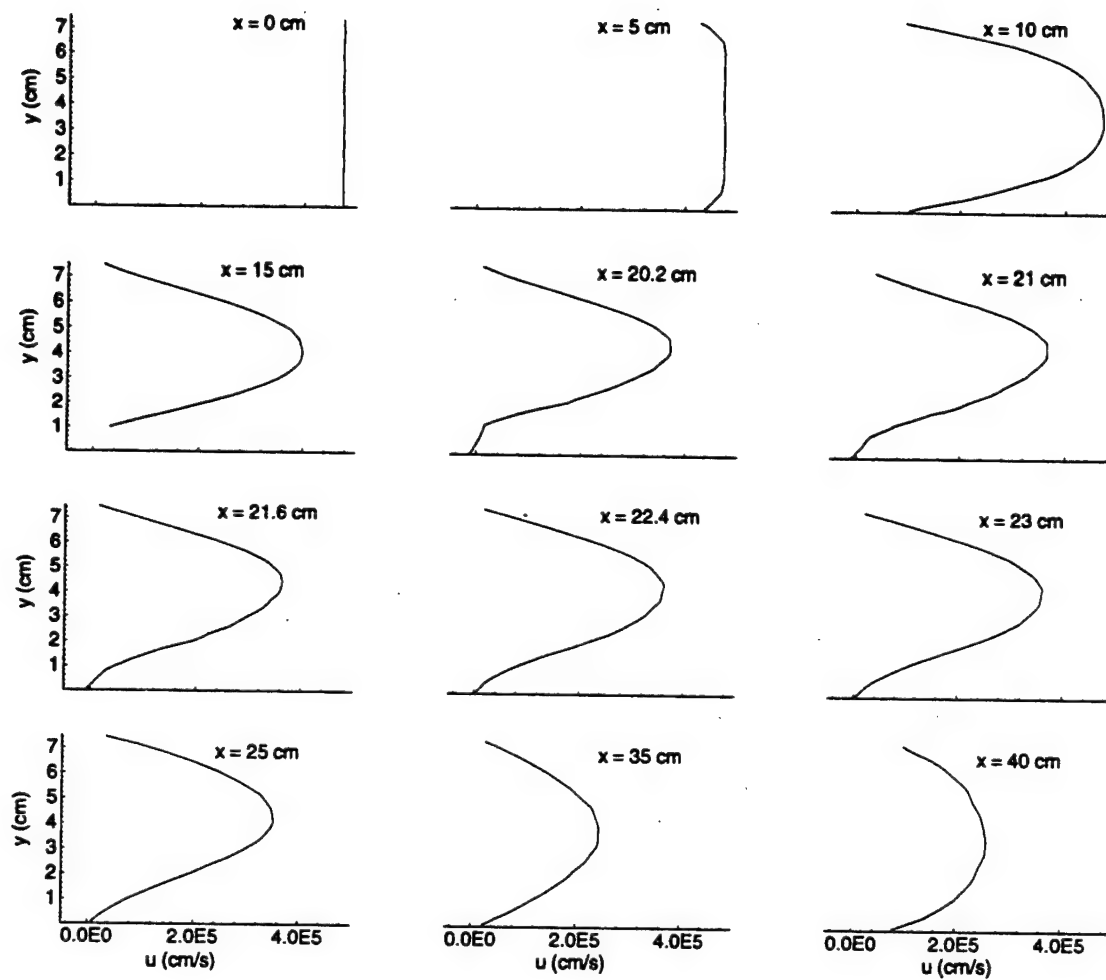
Figure 26: Velocity profiles at various x-locations along the channel.
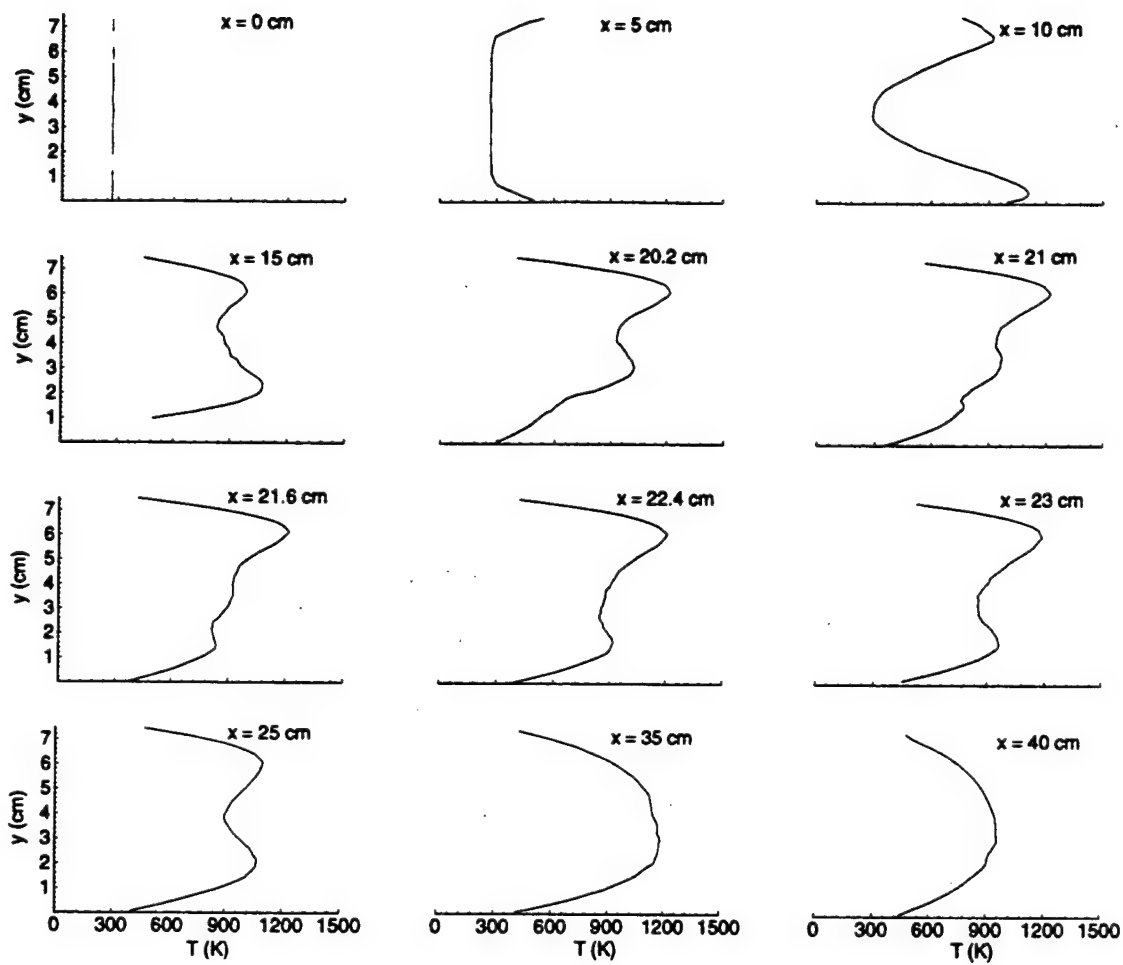
Figure 27: Temperature profiles at various x-locations along the channel.
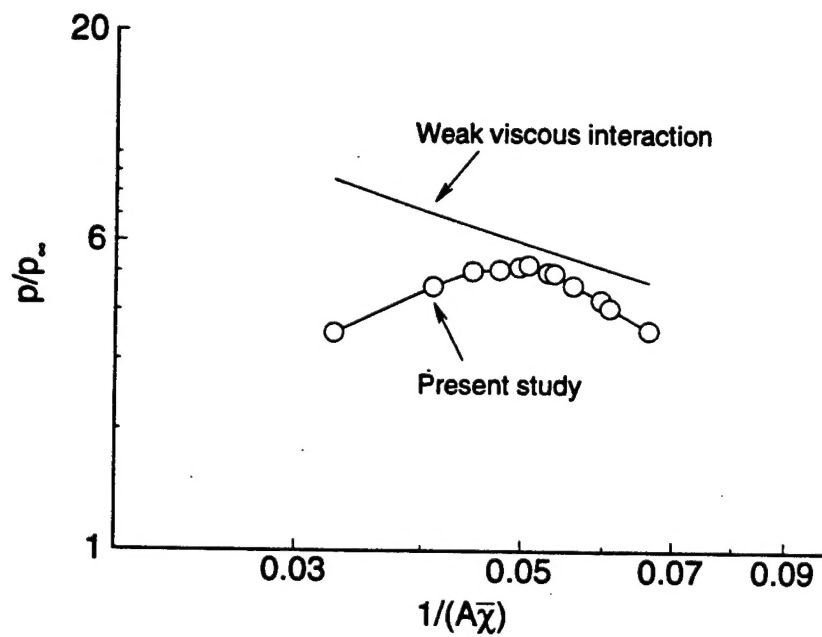
Figure 28: Comparison of calculated normalized pressure distribution near the top leading edge of the channel to that of weak viscous interaction theory. $A = 0.5(\gamma - 1)0.664(1 + 2.6T_w/T_o)$.
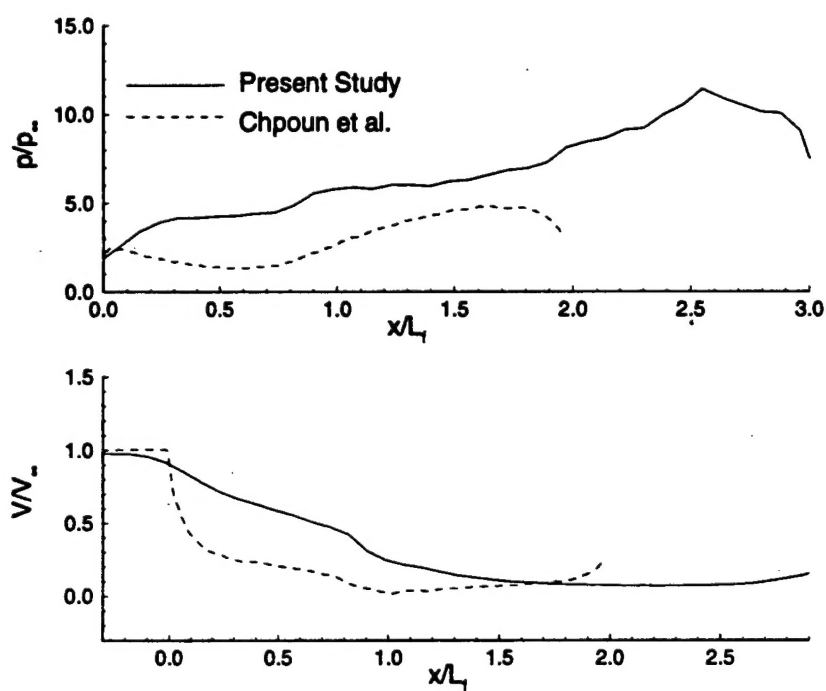
Figure 29: Comparisons of surface properties with data from Chpoun *et al.*, (1993). a) Pressure, b) Velocity.
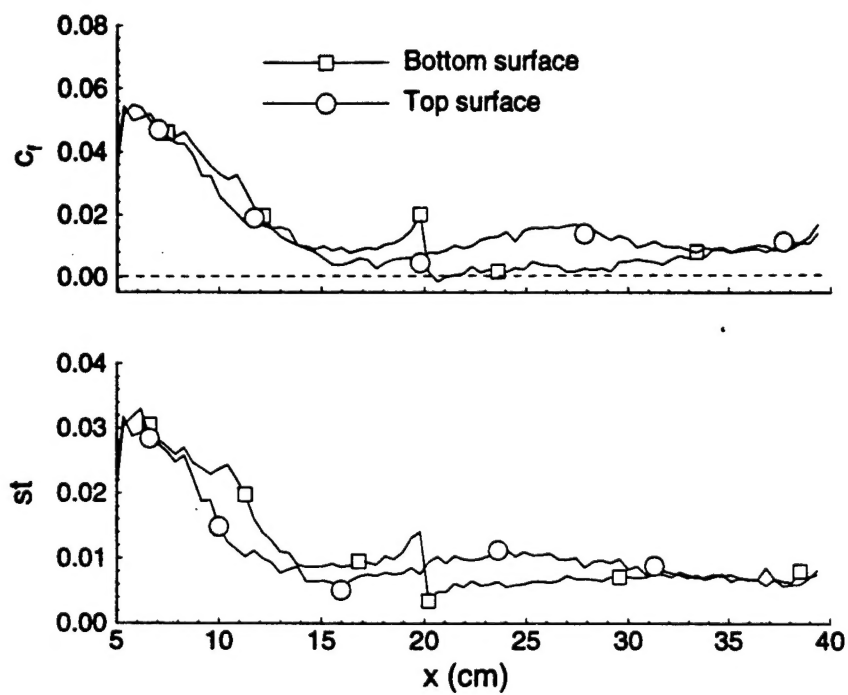
Figure 30: Distributions of skin friction coefficient and Stanton number along the top and bottom surface of the channel.
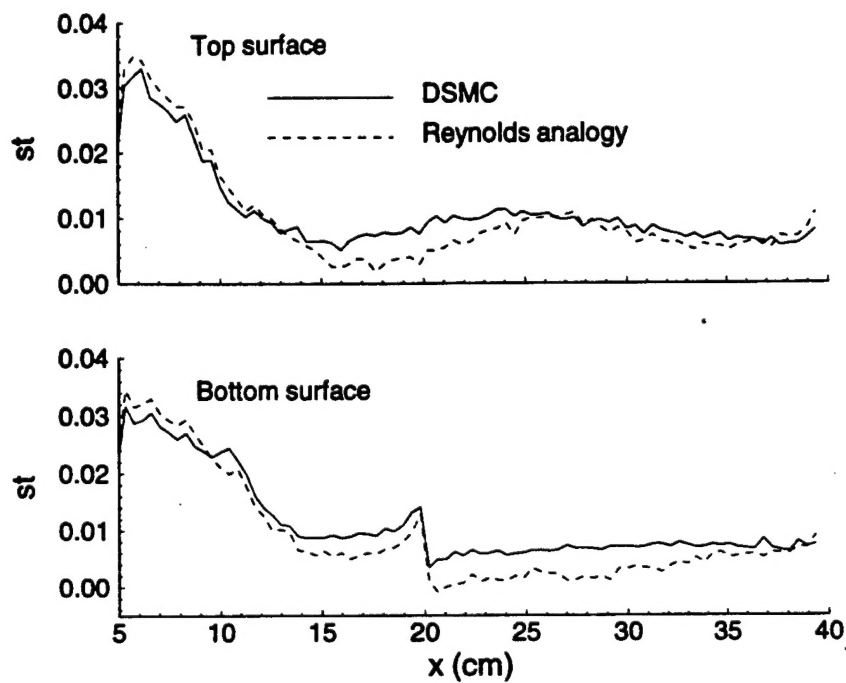
Figure 31: Comparisons of DSMC-calculated and Reynolds analogy Stanton number distributions: a) top surface, b) bottom surface.